2016-06-01

Design and Analysis of Two Compliant Mechanism Designs for Use in Minimally Invasive Surgical Instruments

Jason Lon Dearden
Brigham Young University

Design and Analysis of Two Compliant Mechanism Designs for Use in Minimally Invasive Surgical Instruments

Jason Lon Dearden

A thesis submitted to the faculty of
Brigham Young University
in partial fulfillment of the requirements for the degree of

Master of Science

Larry L Howell, Chair
Brian D. Jensen
Spencer P. Magleby

Department of Mechanical Engineering

Brigham Young University

June 2016

ABSTRACT

Design and Analysis of Two Compliant Mechanism Designs for Use in
Minimally Invasive Surgical Instruments

Jason Lon Dearden
Department of Mechanical Engineering, BYU
Master of Science

Minimally invasive surgery (MIS) has several advantages over traditional methods. Scaling MIS instruments to smaller sizes and increasing their performance will enable surgeons to offer new procedures to a wider range of patients. In this work, two compliant mechanism-based minimally invasive surgical instrument wrist or gripper mechanisms are designed and analyzed.

The cylindrical cross-axis flexural pivot (CCAFP) is a single-degree-of-freedom wrist mechanism that could be combined with existing gripper mechanisms to create a multi-degree-of-freedom instrument. The simplicity of the CCAFP mechanism facilitates analysis and implementation. The flexures of the CCAFP are integral with the instrument shaft, enabling accessories to be passed through the lumen. The CCAFP is analyzed and determined to be a viable wrist mechanism for MIS instruments based on research results. A finite element (FE) model of the mechanism is created to analyze the force-deflection and strain-deflection relationships. Experimental results are used to verify the FE model. A 3 mm design is created that could undergo an angular deflection of $\pm 90^\circ$. The addition of cam surfaces to help guide the flexures and limit the maximum stress during deflection is explored. These cam surfaces can be integral to the instrument shaft along with the flexures. A 2 degree-of-freedom (DoF) CCAFP with intersecting axes of rotation is also introduced.

The inverted L-Arm gripper compliant mechanism has 2 DoF, one wrist and one gripping. Three challenges associated with using compliant mechanisms in MIS instruments are considered: inadequate performance in compression, large flexure deformations, and a highly variable mechanical advantage. These challenges were resolved in the L-Arm design by inverting the flexures, tailoring flexure geometry and employing nitinol, and integrating pulleys into each jaw of the mechanism. The L-Arm was prototyped at several sizes to demonstrate functionality and scalability. A finite element model of the L-Arm flexure was created to determine the strain-deflection relationship. A fatigue test was completed to characterize nitinol for use in compliant mechanism MIS instruments.

These concepts demonstrate the ability of compliant mechanisms to overcome the design and manufacturing challenges associated with MIS instruments at the 3 mm scale. The models and principles included in this work could be used in the application of compliant mechanisms to design new MIS instruments as well as in other areas that employ compliant mechanisms in a cylindrical form factor.

Keywords: compliant mechanism, minimally invasive surgery, cross-axis flexural pivot, nitinol

ACKNOWLEDGMENTS

This research was primarily funded through a grant from Intuitive Surgical, Inc. Some material is partially based on work supported by the National Science Foundation and the Air Force Office of Scientific Research under NSF Grant EFRI-ODISSEI-1240417.

This work was made possible with the support and direction given by many people. I would like to thank Dr. Larry Howell for his time and involvement as my graduate committee chair and Drs. Brian Jensen and Spencer Magleby for their guidance as committee members. Their contributions to this research, help in the preparation of publications, and encouragement are greatly appreciated.

Project direction and feedback from Ryan Steger, Andrew Waterbury, Ted Rogers, and the team at ISI was invaluable in the development of the concepts included in this work and other publications. My experience working with ISI was always positive and professional.

The work of Jordan Tanner and Clayton Grames largely provided the foundation on which this research is based. Their insight was instrumental in the evolution of this research. Jason Orr's assistance in creating test fixtures and running experiments is also recognized.

I thank everyone in the Compliant Mechanisms Research Group for their help with this research as well as keeping me company during my stay in the lab. I'm grateful to have collaborated with such great peers and wish everyone the best.

I am grateful for my family and for the support they have given throughout my education. Their example of sacrifice, hard work, and patience are an inspiration to me. A special thanks goes to my wife Nicole for keeping me on track, editing papers, and being supportive throughout graduate school.

TABLE OF CONTENTS

LIST OF TABLES

LIST OF FIGURES

CHAPTER 1. INTRODUCTION

As advances are made in medical care, minimally invasive surgery (MIS) has emerged as an alternative to traditional surgery. The advantages of MIS include reduced patient trauma, healing time, procedure cost, and error during surgery. It is accomplished using specialized tools that allow surgeons to access the surgical site and manipulate the target through a few small incisions. MIS presents many advantages, but is currently limited to mainly laparoscopic (abdominal) surgeries due to instrument size and site accessibility. Smaller instruments are desired to increase the effectiveness of current procedures and facilitate new procedures including pediatric and eye surgery as well as nerve suturing [1–3]. As the size of instruments used in minimally invasive surgery decreases, new techniques need to be implemented to achieve similar performance as current (larger) instruments. As instruments approach a diameter of 3 mm (instruments less than $\sim$3 mm in diameter are often classified as needlescopic), conventional designs and associated manufacturing processes become less feasible due to physical limitations and increased cost. The minimum possible feature size using conventional processes becomes large relative to the instrument size, potentially reducing performance and increasing manufacturing cost. At such scales friction can cause unpredictable binding and stiction as the friction forces become large in comparison to the mechanism input and output forces. Maintaining or increasing the range of motion while decreasing swept volume is also desirable to allow for use over a wide range of surgical site geometries and procedures. These needs indicate the opportunity to adapt principles of compliant mechanisms to overcome scaling and fabrication issues, leading to decreased instrument size and desired instrument performance.

1.1 Background

Minimally invasive surgery has become a widely accepted method for many routine surgeries, including appendectomies, cholecystectomies, hysterectomies, esophageal reflux surgery,

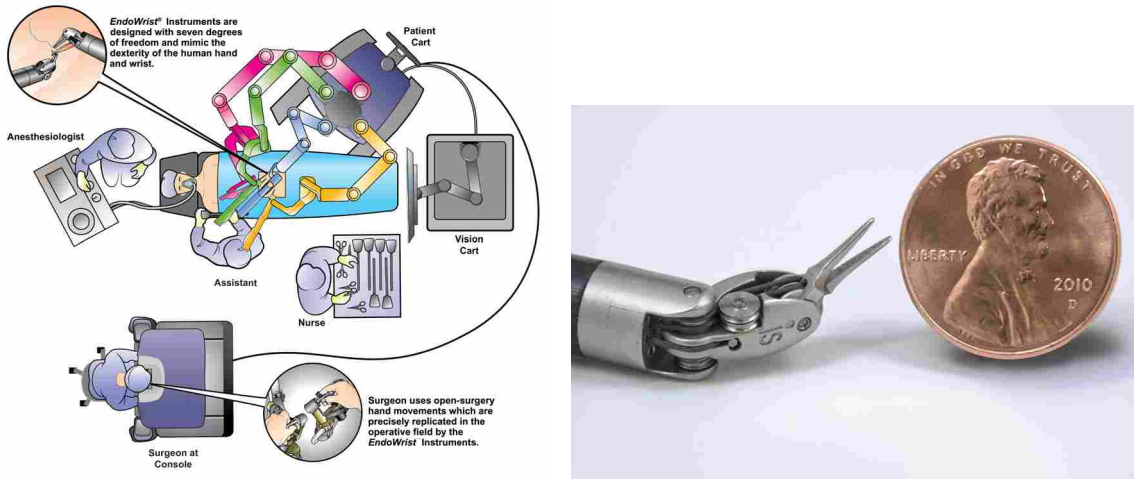

(a) (b)

Figure 1.1: (a) Minimally invasive surgery operating room setup. (b) Representative example of Intuitive Surgical's 8mm Endowrist instruments. © 2016 Intuitive Surgical, Inc.

and colon surgery [4]. The surgical site is viewed through an endoscope, while instruments inserted through other incisions are used to manipulate the target. Advantages of MIS include surgical precision and decreased healing time, both of which potentially contribute to lower healthcare costs. Some patients can be released on the same day the surgery is performed. Manual MIS is accomplished by a surgeon standing over the patient with manually positioned and actuated instruments. Robotic MIS implements a control station at which the surgeon remotely controls the robot-driven surgical instruments. Robotic MIS enables greater dexterity, tremor reduction, and precision (see Fig. 1.1a).

Current MIS instruments are subject to both scaling and manufacturing issues. Pin joints are commonly used in surgical instruments. At the millimeter scale parasitic friction forces associated with the pin joints become large relative to the input and output forces. High friction forces may cause binding and stiction leading to a nonlinear, unpredictable force-deflection relationship. Control algorithms would be difficult to design for such situations. Several manufacturing processes used in surgical instruments include traditional casting and machining. Due to scaling issues, the minimum feature size of these processes becomes large relative to the instrument size and current manufacturing techniques and processes become increasingly costly and less feasi-

ble. Alternative methods and techniques to determine viable processes for manufacturing smaller instruments also need to be explored.

An important consideration in the design of surgical instruments is the volumetric space through which the end effector travels during its full range of motion. This measure, known as swept volume, should be minimized to provide maximum utility. A lower swept volume enables more movement to be carried out in a smaller space.

Most current instruments in the 3 mm (needlescopic) range have one degree-of-freedom (DoF) [5]. Most commercially available robotic surgical devices have three DoF, one gripping and two wrist, but are 5 mm or larger. Maintaining three degrees of freedom while reducing instrument size is desirable.

Extensive research regarding MIS instruments and techniques has been done [4, 6]. There are many examples of instruments on the order of 10 mm in the literature [7–9]. Other research has focused on reducing instrument size [10]. Previous work includes a disposable compact wrist [11], a 5 mm plastic DragonFlex manual laparoscopic instrument [12], and Intuitive Surgical's commercially available Endowrist instruments [13] (as seen in Fig. 1.1b), among others [14, 15].

Research has also been conducted in the area of compliant mechanisms for MIS including a compliant micro-robotic wrist [16], origami-inspired Oriceps [17], a 5 mm multifunctional compliant forceps/gripper [18], and a split compliant rolling contact element (Split CORE) two-degree-of-freedom gripper [19]. Compliant mechanisms are of interest because they can combine motion and structural aspects into the same element, thereby potentially reducing part count and mechanism complexity while maintaining performance. There are several challenges when designing compliant mechanisms including complicated analyses, limited range of motion, and often competing flexibility and rigidity requirements. Despite these challenges, compliant mechanisms have the potential to greatly reduce the size and cost of laparoscopic instruments.

Minimally invasive surgery has many advantages over open surgery. These advantages will continue to become more apparent as instrument size is decreased. This research could potentially lead to commercially viable high-performance needlescopic surgical instruments. Procedures that could not be performed previously would become possible. Patient healing time would be reduced as well as medical costs for both hospitals and patients.

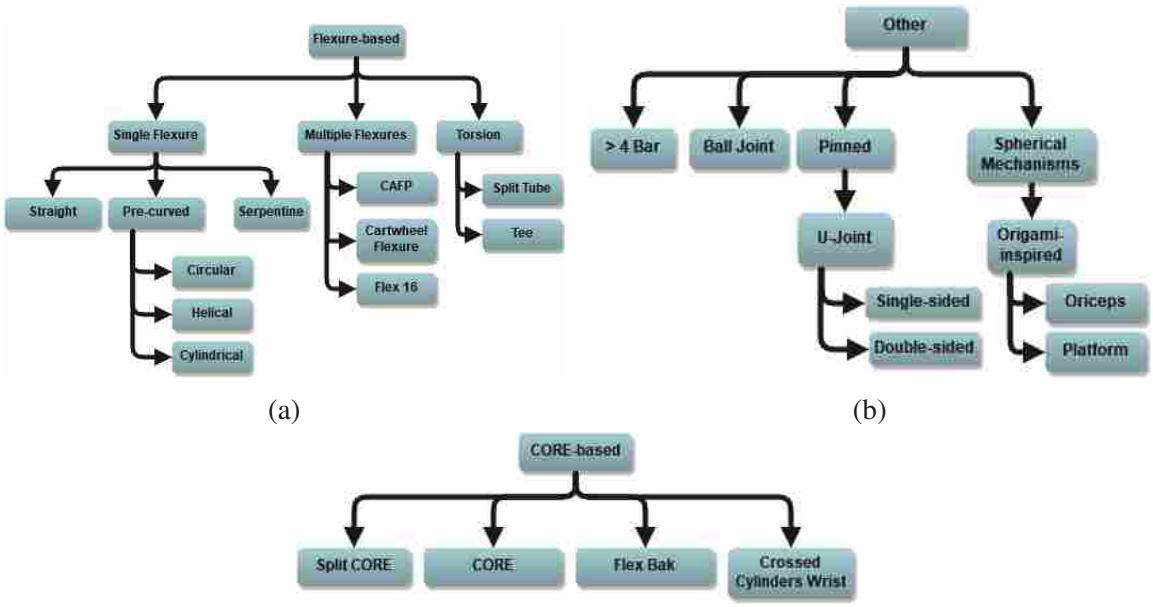

Figure 1.2: Classification trees used to organize wrist and gripper concepts.

1.2 Research Objectives

The objective of this research is to create and analyze two wrist or gripper mechanism designs that could be scaled to 3 mm for use in minimally invasive surgical instruments. Concepts and principles developed in this work could be adapted for use in the design of other MIS instruments. Knowledge of compliant mechanisms and their ability to combine mechanism functions is leveraged as a possible method to achieve such performance. The constraints of MIS are used to guide the exploration of the limits of compliant mechanisms in different configurations, situations, and environments.

1.3 Design Exploration

A design process including concept generation, down selection, concept design, analysis, and experimental testing was used to create and analyze compliant mechanism concepts. Many designs were considered and classified during the concept generation phase of this research (see Fig. 1.2). Of these concepts several were chosen for further exploration, two of which are included in this work. The cylindrical cross-axis flexural pivot (CCAFP) is proposed as a 1 DoF wrist (with the possibility of adaptation as a 2 DoF wrist). The inverted L-Arm compliant mechanism is a

2 DoF gripper. Both designs have the potential to be scaled to the 3 mm size. These designs were selected for their ability to meet manufacturability and performance targets.

The 1 DoF CCAFP wrist mechanism was designed to achieve $\pm 90^{\circ}$ of angular deflection. Several prototypes were created at various scales to demonstrate functionality. The CCAFP design was evaluated using both finite element analysis and experimental validation. A 3 mm CCAFP was created using commercial nitinol tubing and tested to show feasibility. Cam-surfaces intended to control the curvature of the flexure and limit stress in the flexure are introduced. It was determined that they have potential in many applications with further development. (See Chapter 2)

The inverted L-Arm gripper compliant mechanism employs flexures to achieve two degrees-of-freedom, one wrist and one gripping. Three challenges associated with the use of compliant mechanisms in surgical instruments were identified and strategies to overcome them are presented using the L-Arm gripper as an example. Finite element analysis was used to determine the strain-deflection relationship for a nitinol flexure. A mechanical advantage analysis was completed using the pseudo-rigid-body model. Prototypes were created to demonstrate functionality. (See Chapter 3)

This work builds on prior research and is a continuation of an effort to apply principles of compliant mechanisms to the design of surgical instruments [19–22].

CHAPTER 2. CYLINDRICAL CROSS-AXIS FLEXURAL PIVOT

2.1 Introduction

The cross-axis flexural pivot (CAFP) has been studied extensively [23–25]. The CAFP mechanism can replace traditional pin joints, especially in applications where low wear and/or friction are desired such as high-precision positioners [26] and space applications [27].

A traditional cross-axis flexural pivot is made up of two flexures that cross at an angle, often mid-length, between the grounded and output links, as shown in Fig. 2.1. The center of rotation of the CAFP is approximated at the point where the flexures cross. Large deflections can be achieved while maintaining a nearly constant center of rotation.

The cylindrical cross-axis flexural pivot (CCAFP) proposed here is a derivative of the CAFP [28]. The CCAFP consists of a hollow cylinder with two elliptical flexures at an angle, as shown in Fig. 2.2.

The motivation for this work is the use of compliant mechanisms [29] in robotic minimally invasive surgical (MIS) instruments, specifically for the end effector wrist and gripper motions. Most robotic minimally invasive surgical instruments are located on the end of a cylindrical shaft. Cables run the length of the shaft to actuate the instrument. As the size of MIS instruments is decreased new methods are needed to maintain or increase their range of motion and performance. The advantages of compliant mechanisms become more apparent as mechanism size decreases, including lower part count, low wear and friction, and the ability to combine both structural and articular functions in the same part.

Research has been done with regards to compliant mechanisms in minimally invasive surgical applications, including a steerable joint [30], a compliant MIS kidney manipulator [31], compliant forceps [18, 32], and the origami-inspired Oriceps [17].

The ability to accomplish multiple tasks through the same incision is desirable in MIS. The CCAFP is an attractive design for a MIS wrist mechanism because the flexures are located near the

outside surface of the cylindrical shaft, allowing cables and accessories to pass through the center of the shaft. The CCAFP reduces part count and lends itself to several simple manufacturing methods, as discussed later.

In addition to geometry, material properties are also important to consider in the design of compliant mechanisms. Several materials are considered including steel, stainless steel, titanium, and the nickel titanium alloy nitinol (NiTi). NiTi can exhibit the superelastic effect and is therefore of interest in the field of compliant mechanisms. Steel reaches strains of less than 1% before yielding while superelastic NiTi can reach strains of 6-8% with minimal material set. NiTi has been used extensively in medical applications [33]. Bio-compatibility studies have been done that show NiTi components with surface treatment can perform comparable to or better than stainless steel [34,35]. A 2 degree-of-freedom (DoF) 2.5 mm superelastic NiTi wrist mechanism was developed by Sieklicki, et al. [36]. Liu, et al. created a MIS wrist mechanism using superelastic NiTi to obtain a much larger range of motion compared to stainless steel wrists of similar geometries [37].

This paper considers the geometry, force-deflection relationship, the addition of stress-limiting cam-surfaces (hereafter referred to as cam-surfaces) to guide the flexures of the CCAFP, and possible manufacturing methods for the CCAFP mechanism. A parametric finite element model was created to simulate the CCAFP. Several CCAFP prototypes were created using a wire EDM process, including 1.125 in (28.6 mm) steel and 3 mm NiTi mechanisms. A schematic diagram of the CCAFP with labeled geometry is shown in Fig. 2.3.

2.2 CCAFP Finite Element Model

A parametric finite element (FE) model of the CCAFP was created in ANSYS 15.0 using SOLID186 elements and nonlinear geometry. The flexures were modeled with a fixed condition at one end and a rigid coupler connection between the flexures at the other end (see Fig. 2.4). A load was applied using additional geometry, extending from the moving coupler link. Loading conditions included a follower force or a moment couple, both applied as pressures on the model. The load magnitude was varied until the mechanism deflected to the desired angle. Load, rotation, stress, and strain values were taken at each load-step and used to construct the moment-rotation and stress-strain curves. Symmetry was used to halve the number of elements in the model to

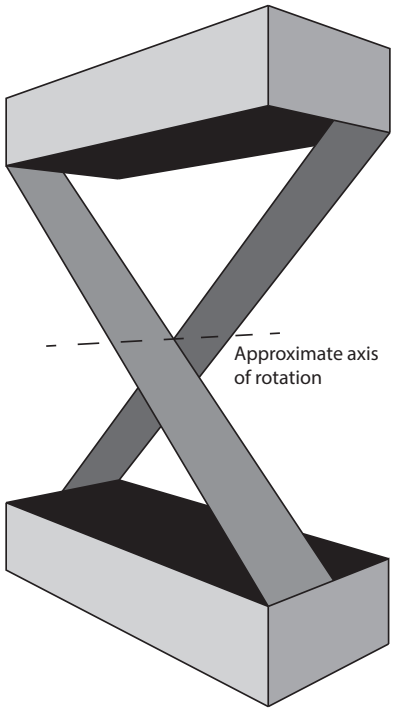

Figure 2.1: A planar cross-axis flexural pivot

approximately 50,000, thus decreasing computation time. The FE model and example results are shown in Fig 2.4.

This model is similar to that developed in [25] except the force-deflection analysis of the CCAFP includes curved beams that constitute the flexures and there is a slight difference in stiffness between inner and outer flexures due to geometry variations.

2.3 Model Verification

The cut pattern for the CCAFP is planar and therefore lends itself to manufacturing using a variety of methods, including laser-cutting, wire EDM, waterjet, and traditional machining, depending on the material used. All CCAFP prototypes described in this paper were created using wire EDM.

Physical prototypes were used to validate the FE model. Hardware was created using standard sizes of 4130 steel tubing. A representative example is shown in Fig. 2.5. Notches at

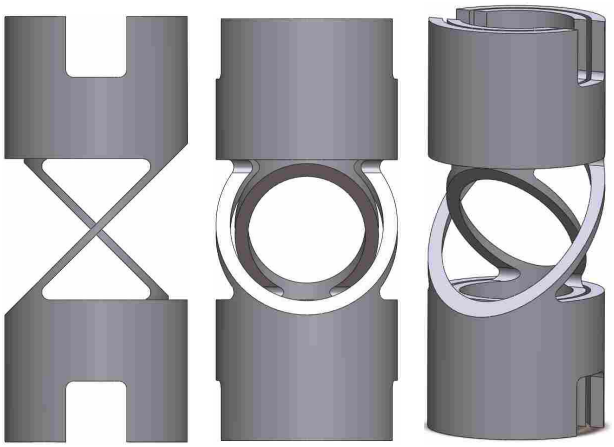

(a) (b) (c)

Figure 2.2: A cylindrical cross-axis flexural pivot showing (a) side, (b) front, and (c) isometric views.

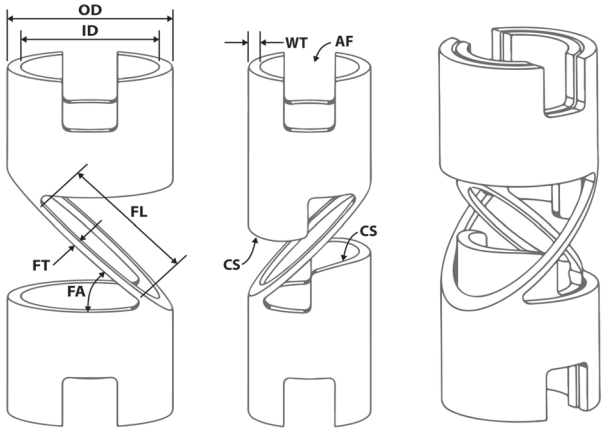

(a) (b) (c)

Figure 2.3: Schematic of a CCAFP showing (a) the outer cylinder where OD is the cylinder outside diameter, ID is the cylinder inside diameter, FL is the flexure length, FT is the flexure thickness, and FA is the flexure angle. (b) the inner cylinder where WT is the wall thickness, AF is an alignment feature, and CS is a stress-limiting cam-surface. (c) the assembled mechanism. Notice that the cam-surfaces are only on the inner cylinder in this particular configuration.

the ends of each cylinder serve as alignment features during assembly and testing. The dimensions of the prototypes are listed in Table 2.1.

Experimental data was collected using the moment-deflection test fixture shown in Fig. 2.6. A calibrated torque sensor measured the reaction moment as the CCAFP was deflected. An optical encoder recorded the angle to which the CCAFP was deflected for each measurement. The FE and

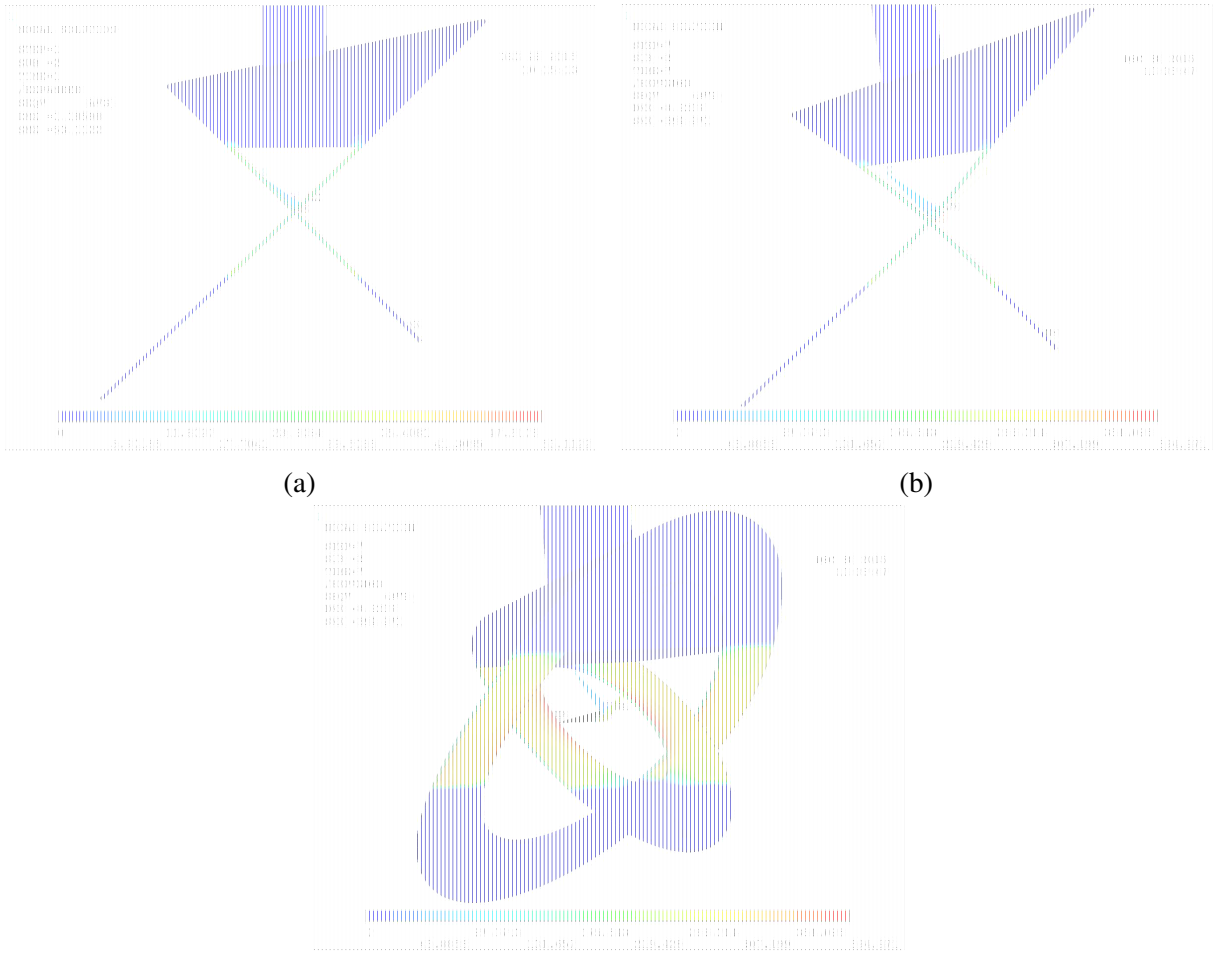

(a) (b)

(c)

Figure 2.4: FE model of the 1.125 in (28.6 mm) 4130 steel prototype displaying the nodal von Mises stress in the flexures in MPa. (a), (b) show a nearly undeflected mechanism and the mechanism deflected to $\sim 9^\circ$, respectively. (c) shows how the elliptical flexures deflect and the location of the highest stress. The maximum von Mises stress in the flexures is 395 MPa at $\sim 9^\circ$.

experimental data are plotted in Fig. 2.7. The FE model and experimental data closely matched. The differences are attributed to test fixture calibration, uncertainty in the material properties, and uncertainty in loading conditions.

The CCAFP was observed to have a much higher off-axis stiffness than a comparably sized planar CAFP due to the elliptical geometry of the CCAFP flexures.

Figure 2.5: CCAFP made of 4130 steel. The outer cylinder OD is 1.125 in (28.6 mm). The height of each cylinder is approximately 2 in (51 mm).

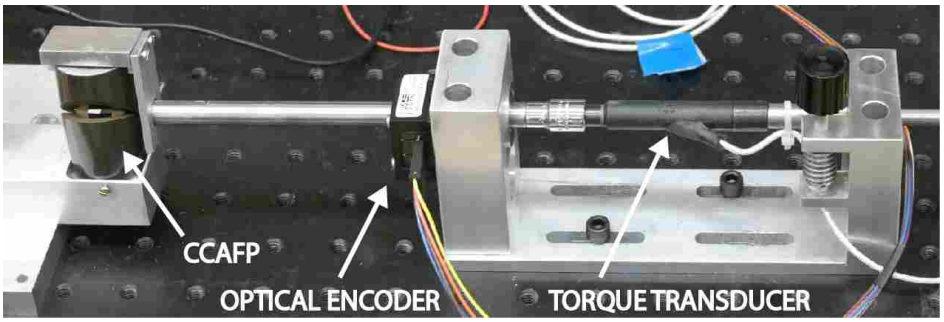

Figure 2.6: Moment-rotation measurement fixture for 1.125 in (28.6 mm) CCAFP prototypes.

2.4 Cam-guided CAFP

Controlling the curvature of a flexure can enable a larger deflection before the flexure yields. For thin, elastic beams, bending moment (and therefore stress) is proportional to curvature and inversely proportional to the radius of curvature. The derivation of flexure stress with respect to the radius of curvature follows the approach described in [38].

Table 2.1: 1.125 in (28.6 mm) 4130 steel CCAFP cylinder and flexure dimensions.

	inner cylinder	outer cylinder
outer diameter, OD, mm (in)	19.05 (0.750)	28.58 (1.125)
inner diameter, ID, mm (in)	9.50 (0.374)	19.02 (0.749)
wall thickness, WT, mm (in)	4.78 (0.188)	4.78 (0.188)
flexure angle, FA, deg	45.0	45.0
flexure thickness, FT, mm (in)	0.25 (0.0098)	0.25 (0.0098)
flexure length, FL, mm (in)	13.72 (0.54)	13.46 (0.53)

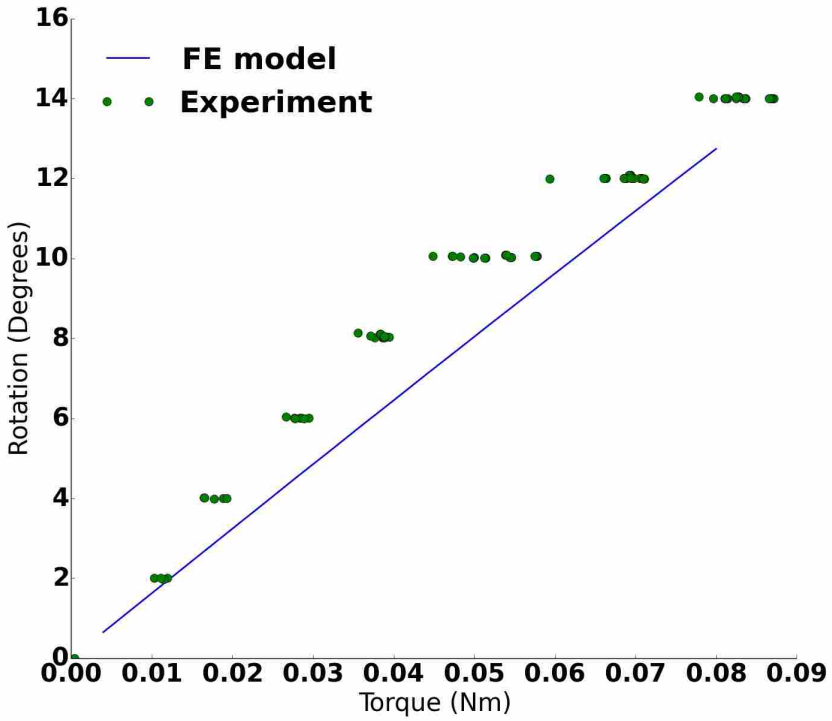

Figure 2.7: Experimental and FE results for a 1.125 in (28.6 mm) CCAFP without cam-surfaces.

The applied moment, M, is related to the controlled radius of curvature, R', as

$$M = \frac{EI}{R'} \tag{2.1}$$

where E is the modulus of elasticity and I is the second moment of area. The maximum stress, σ_{max}, is

$$\sigma_{max} = \frac{Mh}{2I} \tag{2.2}$$

where h is the flexure thickness. Substituting equation (2.1) into equation (2.2) results in the maximum bending stress as a function of the controlled radius of curvature

$$\sigma_{max} = \frac{Eh}{2R'} \tag{2.3}$$

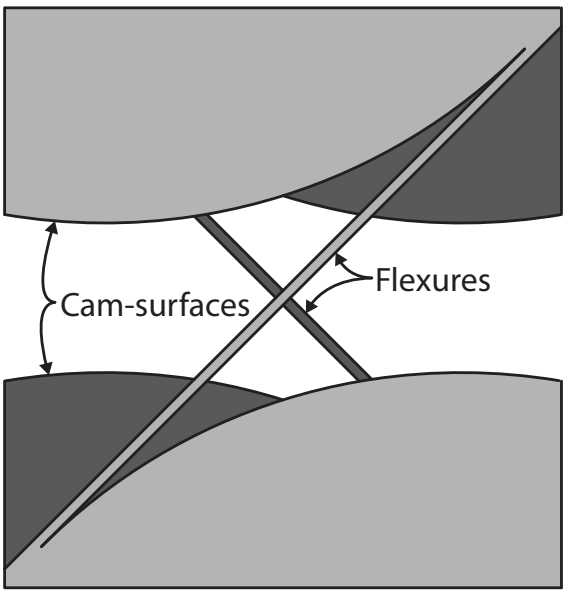

Figure 2.8: Side view of a planar CAFP with stress-limiting cam-surfaces. The approximate axis of rotation is located at the point the flexures cross as shown and is orthogonal to the plane in which the mechanism lies. As the mechanism is deflected the flexures engage the cam-surfaces.

Constraining the radius of curvature of the flexure to be constant results in a constant stress along the member at a given distance from the neutral axis. To control the radius of curvature a cam-surface is integrated into the CAFP design as shown in Fig. 2.8. The ratio of rotation of a CAFP with cam-surfaces to a standard CAFP can be calculated as

$$\frac{\theta_{cam}}{\theta} = \frac{\left(\frac{2S_yL}{Eh}\right)}{\left(\frac{2S_yL\cos\beta}{S_\theta Eh}\right)} = \frac{S_\theta}{\cos\beta} \tag{2.4}$$

where S_y is the yield strength of the material, L is the flexure length, β is the flexure angle, and S_θ is the stress coefficient as defined in [25]. When the flexure angle is 45° (corresponding to $n = 1$ in Jensen, et al), $\frac{\theta_{cam}}{\theta} = 1.36$, meaning a CAFP mechanism with a cam-surface to guide the flexures will theoretically have a 36% increase in angular deflection until yield compared to a standard CAFP of similar geometry. This increased performance may be useful in a variety of applications. The cam-surface may also help carry high compressive loads while the CAFP flexure is engaging it, similar to how a compliant rolling contact element (CORE) joint functions [39].

2.4.1 Cam-guided CCAFP

The flexures of the CCAFP are elliptical segments defined by the cylinder diameter and flexure angle. As a first approximation of the flexure length, the straight-line distance of the flexure based on the inner diameter is used. The straight-line approximation of the flexure length, L, is

$$L \approx \frac{D_i}{\cos\beta} \tag{2.5}$$

where D_i is the inner diameter of the inner cylinder and β is the angle of the flexure from a plane cutting the cylinder orthogonal to the axis of the cylinder. Flexure length is constrained by the inner diameter of the inner cylinder. The flexure in the outer cylinder is designed to be the same straight-line length as the inner cylinder to maintain approximate flexure symmetry. This is done by adding a fillet with a larger radius to each side of the outer flexure (Figure 2.9 shows the difference between inner and outer flexure fillets). The approximate length, L, can then be used to calculate the theoretical angular deflection, θ_{cam}, as

$$\theta_{cam} = \frac{2S_yL}{Eh} \tag{2.6}$$

where S_y is the yield strength of the material, E is the modulus of elasticity, and h is the flexure thickness. Equations 2.3 and 2.6 were used to calculate the radius of curvature of the the cam-surface for the steel prototypes.

Due to the flexure's elliptical shape it will not be in complete contact with the cam-surface during deflection. The moving platform of the mechanism, including a portion of the flexure, begins to exit the boundary defined by the cylinder surface and therefore does not engage the cam-surface. If the flexure is rotated beyond this point it will yield (leading to flexure failure if yielding is not desired). This issue is more apparent when the wall thickness of the cylinder is small compared to the cylinder diameter.

A CCAFP with integrated cam-surfaces was prototyped as shown in Fig. 2.9. In this case the cam-surfaces are located on the inner cylinder. Because the outer flexure is slightly longer than the inner flexure, the highest stress will be developed in the inner flexure for a given deflection (Note that in Table 2.1 the flexure length is the straight-line approximation. When the elliptical shape of the flexure is considered the inner flexure will have a slightly shorter effective flexure

Figure 2.9: 4130 steel CCAFP with cam-surface integrated in the inner cylinder.

length compared to the outer cylinder.) By limiting the stress on the inner flexure the highest stress of the mechanism will be limited. The cam-surfaces could also be located on the outer flexure and a prototype was made in this configuration as well (not shown). Because the inner flexure is usually the stress-limiting member, the cam-surfaces of the outer flexure should be designed with the stress of the inner flexure as the limiting factor. Depending on the angle of rotation and the design of the cam-surfaces, it may not be possible to integrate cam-surfaces on the inner and outer cylinders simultaneously due to interference during actuation. There is no interference if the cam-surfaces are added to only the inside or the outside flexures.

Data collected for the 4130 steel CCAFP prototypes using the moment-rotation test fixture is shown in Fig. 2.10. There is a difference in stiffness between the prototype with the cam-surfaces on the outside cylinder and the CCAFP without cam-surfaces. It is expected that the introduction of cam-surfaces may modify the mechanism stiffness because the flexure curvature is constrained. The data from the prototype with cam-surfaces on the inner cylinder closely matches the data from the CCAFP with no cam-surfaces. Due to how the cam-surface was manufactured the flexure just begins to contact the cam-surface as it reaches its most deflected position. The cam-surface may not modify stiffness; it is acting as more of a hard-stop than a guiding surface in this case.

2.5 Materials Considerations

The performance of compliant mechanisms is affected by the material used. The yield-strength-to-modulus ratio, $\frac{S_y}{E}$, is often used to compare linear elastic materials for use in compliant mechanisms. A high ratio usually indicates good compliant characteristics. Stainless steel is com-

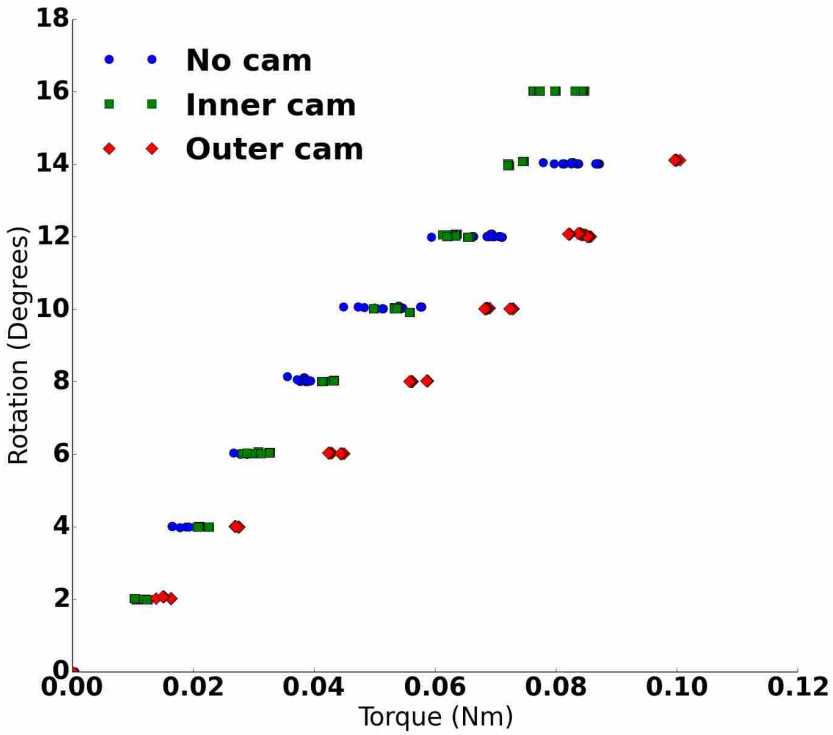

Figure 2.10: Moment-rotation results for a 1.125 in (28.6 mm) CCAFP mechanism with inner, outer, and no cam-surface.

monly used in MIS applications and was therefore chosen as one potential material for the CCAFP. Finite element analysis of a 3 mm diameter stainless steel CCAFP showed a maximum elastic deflection of ± 2.6 degrees for SS304 and ± 12.5 degrees for SS17-4. A Ti-6-4 titanium CCAFP was also analyzed and resulted in a maximum elastic deflection of ± 14.2 degrees. Results for stainless steel and titanium are shown in Fig. 2.11. Yield strengths for the three alloys considered are also shown with dashed lines. While this may be suitable in some applications, the intent of this research was to create a 3 mm design with rotations approaching $\pm 90^{\circ}$.

2.6 Superelastic NiTi

The nickel titanium alloy often known as nitinol exhibits interesting characteristics that may be useful in a variety of applications involving compliant mechanisms. The NiTi alloy can be chosen so that it is superelastic at room temperature and above. The superelasticity of NiTi is due to

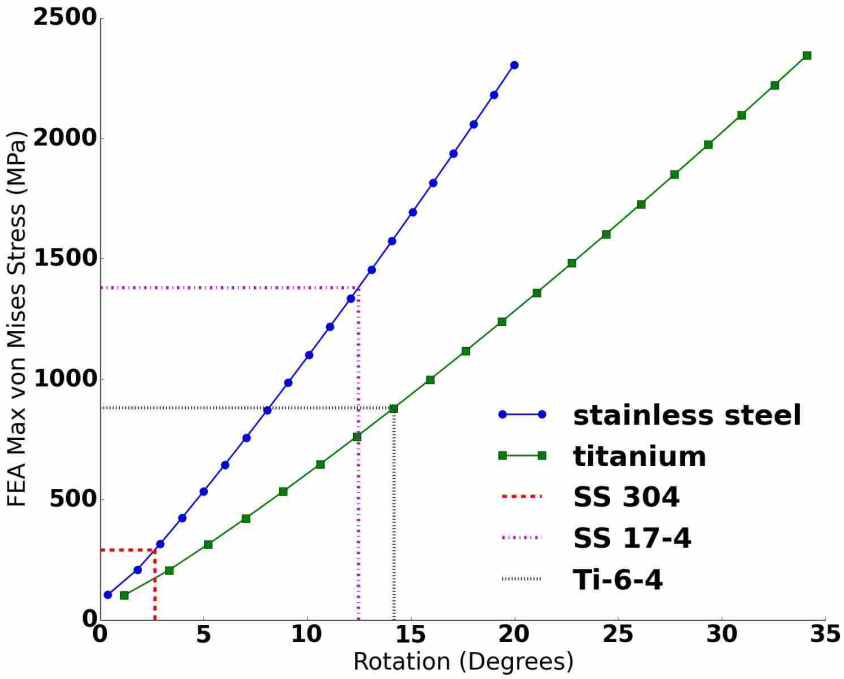

Figure 2.11: Maximum von Mises stress verses mechanism rotation for 3 mm steel and titanium CCAFPs without cam-surfaces. The yield conditions for several alloys are shown.

the austenite-martensite phase transformation that occurs when the alloy is mechanically stressed beyond a certain point [40]. NiTi can be strained beyond 6% without plastically deforming in many situations, while most steels will typically yield at strains of less than 1%. This superelastic behaviour enables a greater range of motion when compared to linear elastic materials for a given mechanism geometry.

NiTi has a nonlinear stress-strain curve with hysteresis. Due to the nonlinear stress-strain response of NiTi, the yield strength is not well defined. Strain is often used as a measure for relative comparisons between designs. For a 4% maximum material strain the mechanism is predicted to undergo 100,000 cycles before failure. A mechanism with 6% maximum strain should undergo about 100 cycles before failure [41].

This nonlinear behavior is often difficult to model and may be undesirable for a force-loaded mechanism. Deflection-loading would be a preferable method of loading, such as the cable actuation commonly found in robotic surgical instruments.

The parametric FE model was updated to include a superelastic material model of NiTi. The loading condition was changed to a single follower force located ~ 3 mm from the pseudo-pivot. Material property values used in the analysis are listed in Table 2.2. The modulus of elasticity of the austenite phase, E, was determined from experimental data as described below. All other values were taken from the literature where μ is Poisson's ratio, σ_s^{AS} is the starting stress value of the forward phase transformation, σ_f^{AS} is the final stress value of the forward phase transformation, σ_s^{SA} is the starting stress value of the reverse phase transformation, σ_f^{SA} is the final stress value of the reverse phase transformation, $\overline{\varepsilon}_L$ is the maximum residual strain, and α is the material response ratio between tension and compression [42].

The FE model was used to compare the relative performance of the CCAFP mechanism at three instrument diameters: 3, 5, and 8 mm using the dimensions in Table 2.3. Figure 2.12 shows a representative example of 3 mm CCAFP with strain contours. Total (elastic + transformation) von Mises strain was plotted against rotation for each instrument size. The results are shown in Fig. 2.13. The maximum von Mises stress developed in the flexures was also plotted against the mechanism rotation as shown in Fig. 2.14.

Superelastic NiTi is available in wire, rod, tubing, strip, and sheet. NiTi alloys can be cut using a laser cutter or wire EDM. Conventional machining can be difficult due to the large strains developed in the material. The 3 mm mechanism was manufactured using hollow NiTi cylinders from Minitubes using a wire EDM with a 0.254 mm (0.01 in) kerf width. One such CCAFP can be seen in Fig. 2.15. The dimensions of the 3 mm NiTi prototypes are found in Table 2.3. The

Table 2.2: Superelastic NiTi material properties used in the FE model with nonlinear properties. Only E and μ were used in the linear material model.

Property	Value
E	21.38 GPa
μ	0.3
σ_s^{AS}	339.0 MPa
σ_f^{AS}	440.95 MPa
σ_s^{SA}	185.5 MPa
σ_f^{SA}	112.6 MPa
$\overline{\varepsilon}_L$	0.048
α	0

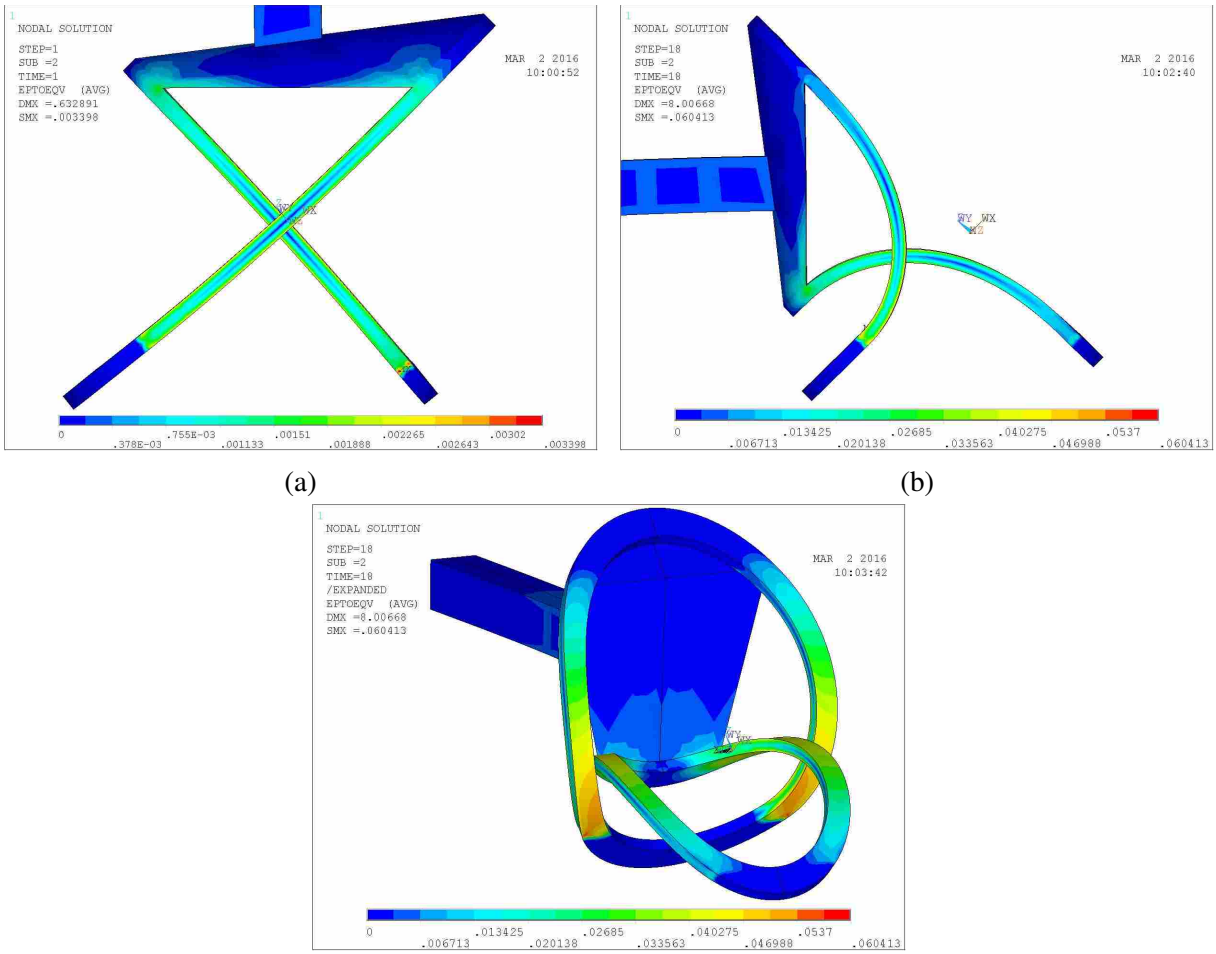

Figure 2.12: FE model for the 3 mm NiTi prototype with linear material properties showing the von Mises total strain for (a) a nearly undeflected mechanism and (b) the mechanism deflected to $\sim 87°$. (c) shows how the elliptical flexures deflect and the location of the highest strain. The maximum von Mises strain is 6.04% at $\sim 87°$.

flexure lengths of the actual prototypes differed from model dimensions due to fillets that were added to reduce stress concentrations. The actual flexure lengths for the inner and outer flexures are 2.551 mm and 2.547 mm, respectively. The cam-guided versions were designed to undergo a 90° angular deflection in each direction from the undeflected position. The heat-affected zone from the wire EDM may affect the material characteristics, especially fatigue life.

Due to the planar wire EDM manufacturing method and the geometry of the cut made in the cylinder, the CCAFP flexures have a non-constant cross section. This will likely affect the input load needed to rotate the flexure and may influence the location of the center of rotation.

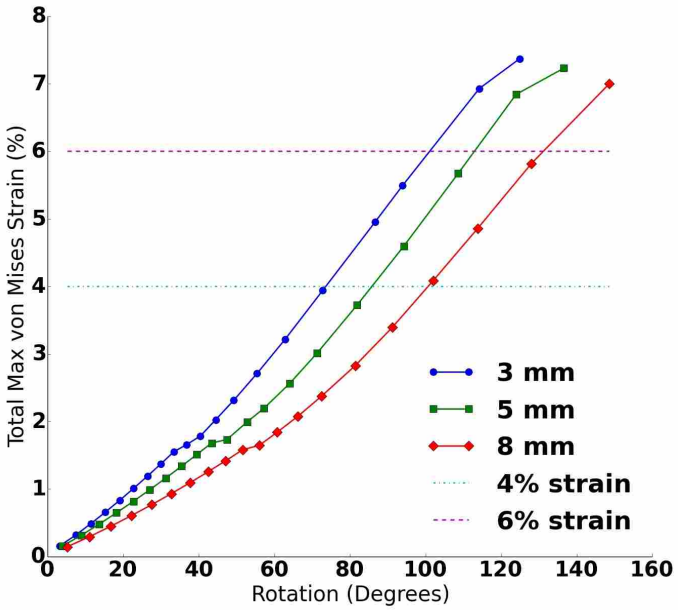

Figure 2.13: Maximum total von Mises strain (elastic and transformation strain) plotted against mechanism rotation angle for 3, 5, and 8 mm NiTi CCAFP mechanisms using a nonlinear material model.

The variation in the cross section occurs parallel to the axis of rotation; the flexure thickness is constant while the flexure width changes along the length of the flexure. Cylinders with a thin wall thickness will have less variation in the flexure width.

A 3 mm NiTi CCAFP was assembled using Kapton shims to align the inner and outer cylinders concentrically (see Fig. 2.16). The cylinders were fixed together using cyanoacrylate

Table 2.3: 3, 5, and 8 mm diameter mechanism cylinder and flexure dimensions. IC and OC indicate the inner and outer cylinder, respectively. Cylinder dimensions are based on commercially available tubing sizes.

	3 mm		5 mm		8 mm	
	IC	OC	IC	OC	IC	OC
outer diameter, OD, mm	2.374	3.001	4.798	5.499	6.998	7.998
inner diameter, ID, mm	1.944	2.533	4.041	4.900	6.099	7.323
wall thickness, WT, mm	0.215	0.234	0.378	0.300	0.450	0.338
flexure angle, FA, deg	45.0	45.0	45.0	45.0	45.0	45.0
flexure thickness, FT, mm	0.125	0.125	0.220	0.220	0.261	0.261
flexure length, FL, mm	2.749	2.749	5.715	5.715	8.625	8.625

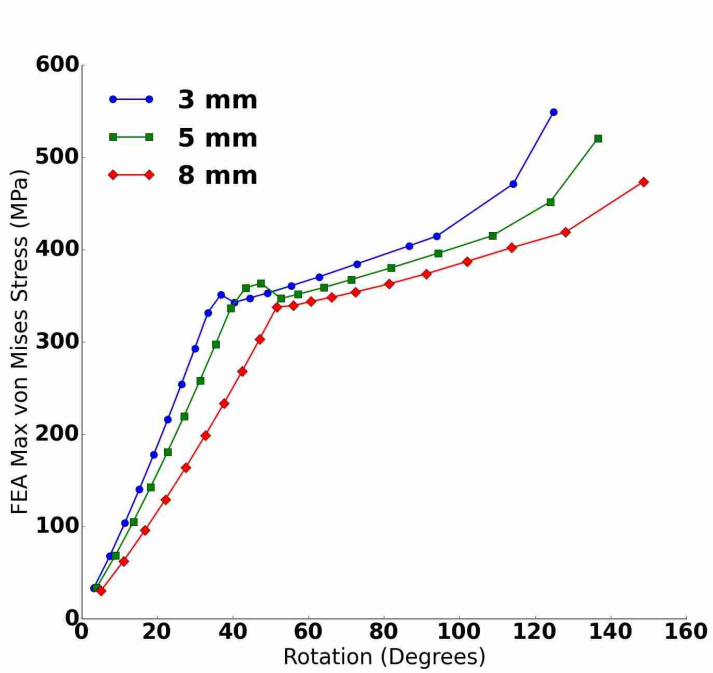

Figure 2.14: Maximum von Mises stress plotted against mechanism rotation angle for 3, 5, and 8 mm NiTi CCAFP mechanisms using a nonlinear material model.

Figure 2.15: 3 mm NiTi CCAFP with ruler for scale. The ruler marks are spaced at 1 mm.

adhesive (see Fig. 2.17). The CCAFP was deflected while viewed under a microscope to verify mechanism functionality as shown in Fig. 2.18.

The 3 mm CCAFP concept was tested using a custom test fixture with a Futek 4.45 N (1 lb) load cell to measure the force required to deflect the mechanism. The test fixture was designed to

Figure 2.16: 3 mm NiTi CCAFP with Kapton shims before bonding the inner and outer cylinders.

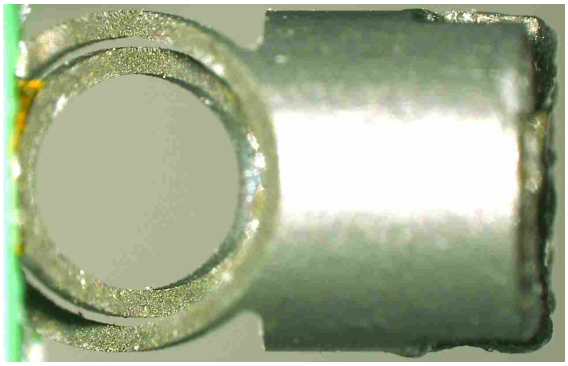

Figure 2.17: 3 mm NiTi CCAFP in its undeflected position as shown from the side looking through the elliptical flexures. The CCAFP is held in a fixture on the left. The gap between inner and outer flexures can clearly be seen as well as the surface finish of the flexures due to the wire EDM process.

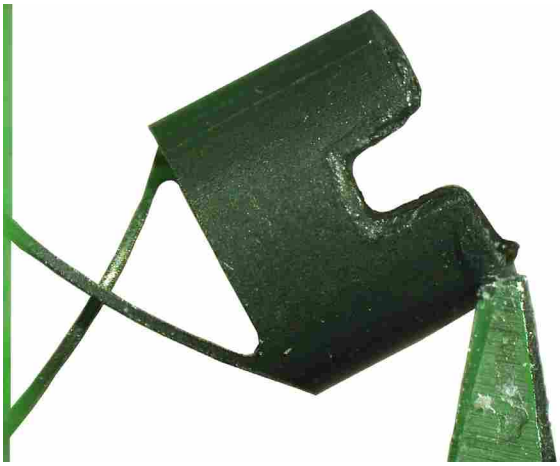

Figure 2.18: A 3 mm NiTi CCAFP in a deflected state.

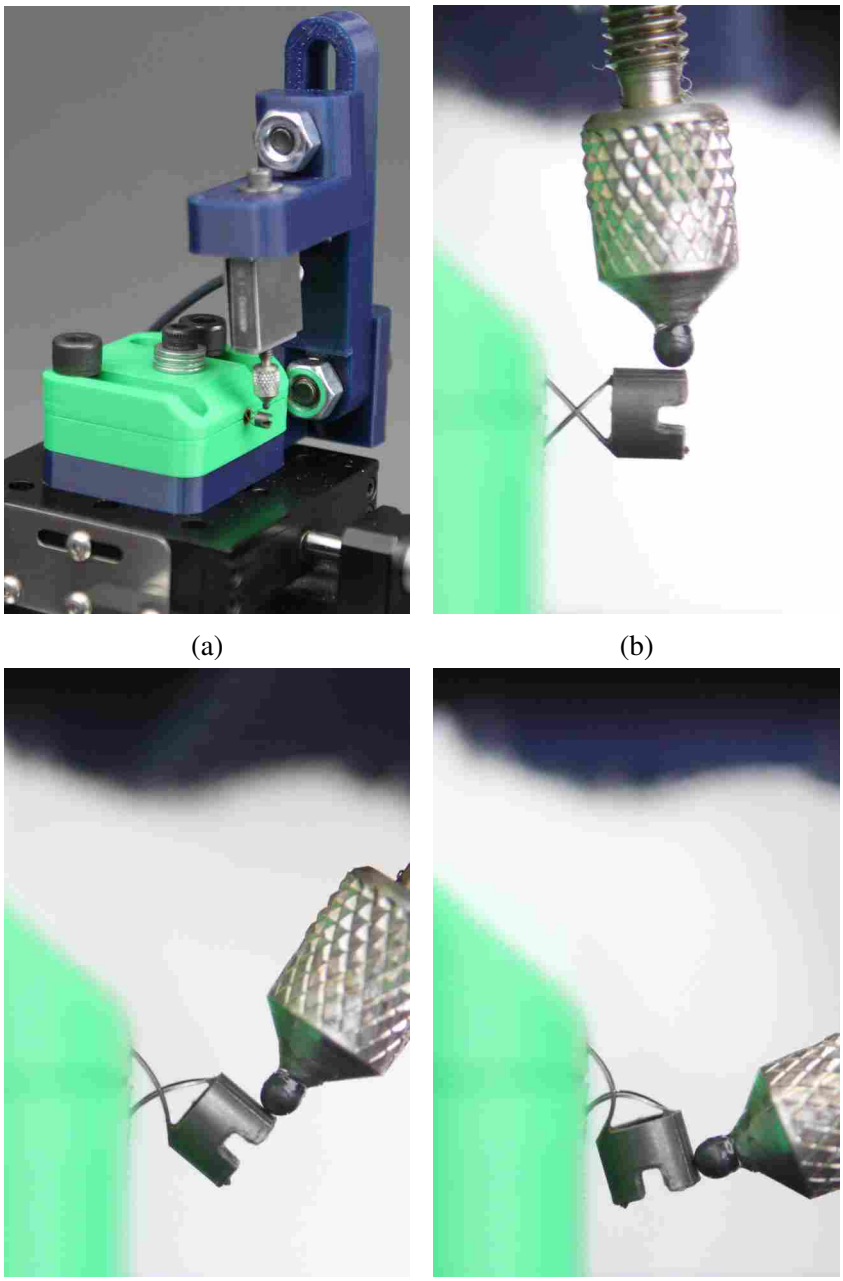

(a) (b)

(c) (d)

Figure 2.19: (a) Test fixture with 3 mm NiTi CCAFP. (b)-(d) CCAFP deflected through several angles.

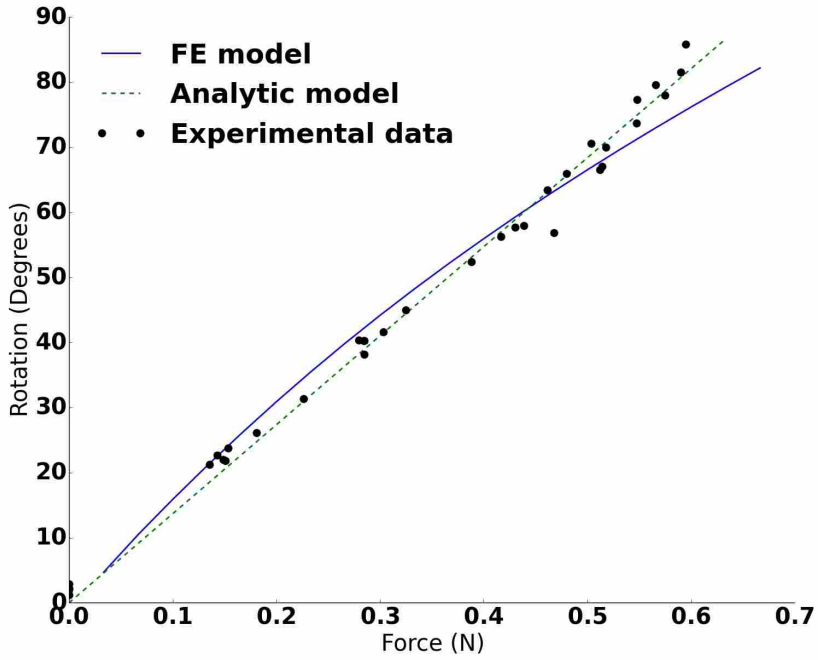

Figure 2.20: 3 mm NiTi experimental data with analytic and FE model

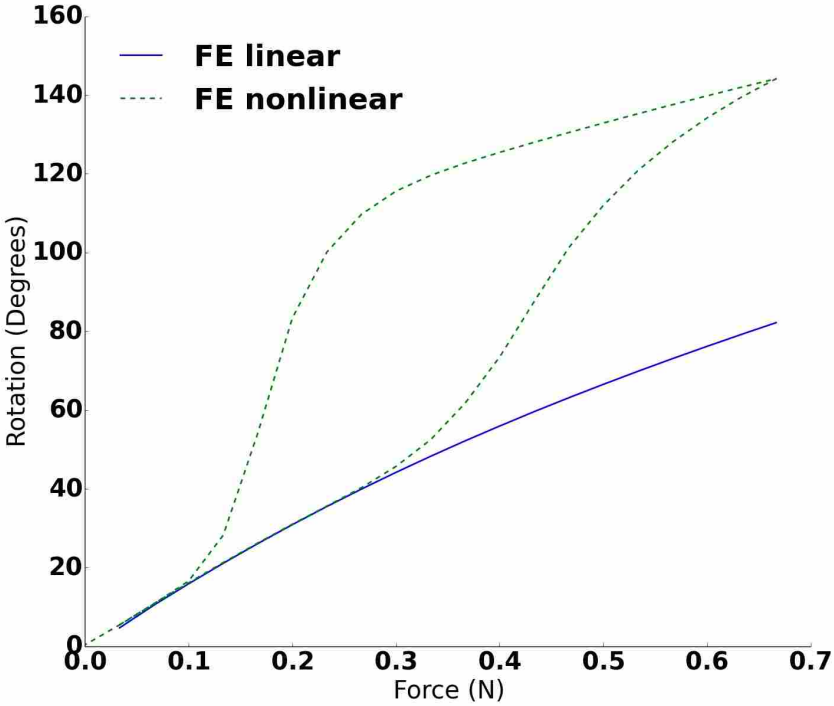

Figure 2.21: 3 mm NiTi FE model with linear and nonlinear material properties.

apply a follower force on the rotating end of the mechanism. The test fixture is shown in Fig. 2.19a. Figures 2.19(b)-(d) show the mechanism as it is deflected through several angles.

Experimental data was collected for a CCAFP without cam-surfaces up to an angular deflection of approximately 85°. Due to mechanism symmetry these results are applicable to both rotation directions. These data suggest a linear relationship between the input force and rotation of the mechanism. Using a least squares linear fit with an intercept at zero, the slope, $\frac{\theta}{F}$, was calculated. The approximate modulus of elasticity was calculated using the slope and the model for CAFP stiffness, K, described in [25] where

$$K = \frac{K_\theta EI}{2l} \tag{2.7}$$

Using a pseudo-rigid-body model similar to that described in [25, 43] and approximating the CCAFP as a pin joint, the relationship between the angular deflection of the joint and the applied moment is

$$\theta = \frac{M}{2K} \tag{2.8}$$

A 2 appears in the denominator because the CCAFP is effectively two CAFP mechanisms in parallel, with double the stiffness of a single set of flexures. Rearranging for the modulus of elasticity, E, the equation becomes

$$E = \frac{Frl}{\theta K_\theta I_{avg}} \tag{2.9}$$

where F is the applied force, r is the perpendicular distance from the pseudo-pivot to the applied force (the moment arm), l is the flexure length, and I_{avg} is the average second moment of area of the flexure. An average value of I was used because the flexure widths of the inner and outer flexures are slightly different, as well as the fact that the flexure width changes as a function of position along the flexure due to the elliptical geometry. Note that the original model assumes a pure moment is applied to the CAFP. For this analysis an approximate moment was applied as a force at a distance.

The modulus of elasticity calculated using experimental data and equation 2.9 was used in the FE model. The experimental data are in good agreement with both the analytic and FE models

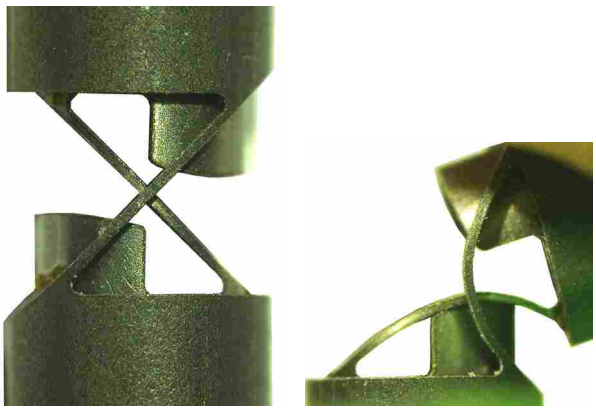

(a) (b)

Figure 2.22: 3 mm NiTi CCAFP with cam-surfaces on the inner flexure. (b) shows the inside flexure engaging the cam-surface.

using linear material properties (see Fig. 2.20). The differences can be attributed to a non-ideal (non-rigid) fixture used for the experimental setup, and uncertainty in the material properties for the FE model. Other than the E determined experimentally, the other material properties were taken from the literature. The heat affected zone created during processing with the micro wire EDM could affect the material properties. As described in [44], a short heating may decrease the stiffness in the material and cause the force deflection curve to more closely approximate a linear relationship.

Figure 2.21 is a plot of the FE model with linear and nonlinear material properties. This shows that the nonlinear material properties of NiTi may enable larger rotations for a given input force. Note that nonlinear material properties of NiTi cause hysteresis in the force-deflection relationship.

2.6.1 NiTi CCAFP with Cam-Surfaces

Figure 2.22 shows a 3 mm CCAFP prototype with cam-surfaces. To avoid interference that can occur between the inner and outer cylinders when both have cam-surfaces, only the inner flexure was manufactured with a cam-surface. Although no cam-surfaces are on the outer cylinder, the cylinder's motion is still constrained by the inner cylinder cam-surfaces. For a CCAFP with no cam-surfaces, the inner flexure develops the highest stress because it has a slightly shorter length

than the outside flexure. Adding cam-surfaces to both inner and outer flexures will reduce the stress in each, but the inner flexure will still develop a higher stress than the outer flexure.

2.7 2 DoF CCAFP with Intersecting Axes of Rotation

Two single DoF CCAFP mechanisms could be stacked in series with their axes of rotation orthogonal to one another to create a two DoF wrist joint. This idea has been previously documented [28], but one potential drawback of this method is that the axes of rotation of the two mechanisms are offset from each other by a distance equal to at least the height of a single CCAFP mechanism, and therefore the swept volume of the joint as a whole is higher than if the axes intersected one another.

The CCAFP design was modified to position the orthogonal axes of rotation so they intersect at the center of the mechanism. This enables two-degree-of-freedom motion with a small swept volume. The prototype shown in Fig. 2.23 was created to demonstrate functionality of the concept.

This new concept could be useful in a variety of applications including an MIS wrist, shaft coupler, or universal joint. Analysis similar to that used in the single DoF CCAFP could be used to determine the performance of this concept for a given set of parameters.

2.8 Conclusion

The CCAFP mechanism was modeled, prototyped, and tested at several scales and in multiple materials. A parametric FE model of the CCAFP was created and verified by experiment. A 3 mm NiTi CCAFP design was created that achieved deflections of $\pm 90^\circ$. Further testing needs to be done to characterize the fatigue life of the flexure for the desired rotation. The CCAFP was experimentally tested up to 85° and is in agreement with the model.

Based on this research it appears that the cam-surfaces may only marginally help for small scale flexures that undergo large deflections because the flexure is only in contact with the cam-surface during a small portion of the deflection. Also, as the elliptical flexure deflects, it moves outside the cylindrical boundary surface and complete contact with the cam-surface does not occur. If the width of the flexures is small (corresponding to a small cylinder wall thickness) then the area

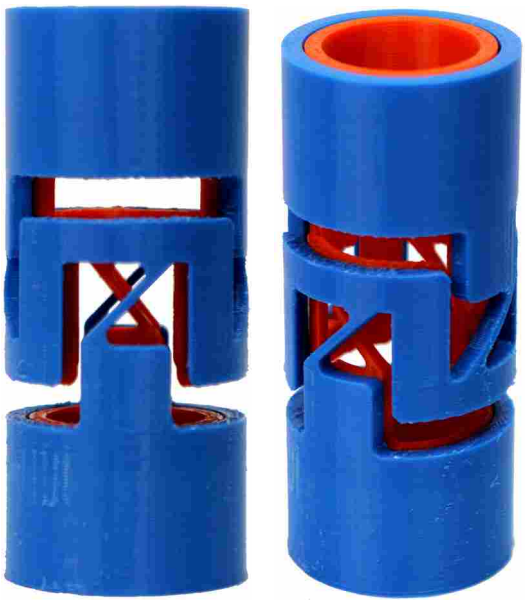

(a) (b)

Figure 2.23: 2 DoF CCAFP prototype with intersecting axes of rotation. Blue and orange PLA was used to differentiate between the inner and outer tubes, respectively.

of the cam-surface in contact with the flexure during deflection will be even smaller. Cam-surfaces used to guide the flexures of a CAFP may be useful at larger scales, or if a small scale mechanisms can be made with a kerf width on the order of the flexure width or smaller.

The CCAFP could be used in a variety of areas including a 1 DoF wrist mechanism, an articulated shaft, or a flexible linkage between rigid cylinders or shafts (flexible shaft-coupler). Two CCAFP mechanisms stacked with axes of rotation orthogonal to each other would create a 2 DoF joint. A 2 DoF CCAFP with intersecting axes of rotation was also created that reduces the swept volume. The combination of traditional compliant mechanisms and cylindrical geometries creates opportunities for further research and application.

CHAPTER 3. INVERTED L-ARM COMPLIANT MECHANISM

3.1 Introduction

Minimally invasive surgery (MIS), an alternative to traditional surgery, has several benefits including less patient trauma, decreased procedure time, and little to no scarring due to the small size of the incisions [45]. As advances in MIS are made these potential benefits will become more apparent and procedures not previously possible will become more feasible. One way to advance MIS is to scale instruments to smaller sizes, thus facilitating smaller incisions and more intricate procedures. Current instruments present some issues when scaled to smaller sizes, including in their design and manufacturing. As the size of MIS instruments is decreased, new methods are needed to retain or increase instrument range of motion and performance.

The use of compliant mechanisms in minimally invasive surgery devices is attractive for reasons that include an ability to scale designs, reduce or even eliminate assembly, assure precise motion, and reduce part count, friction, and wear [29]. The motivation for this research is to demonstrate the use of compliant mechanisms in robotic MIS instruments, specifically to achieve end-effector wrist and gripper motion.

Although compliant mechanisms show promise for advancements in minimally invasive surgery, three challenges accompany their development for use in grippers:

1. Preload in cable-actuated systems induce compressive loads on components, but compliant members generally perform inadequately in compression [46].

2. For the $\pm 90^{\circ}$ range of motion desired for each jaw, the resulting bending stresses in the flexures are too high for materials used in current instruments.

3. The moment arm for cables attached at fixed points on the mechanism will cause a changing and diminishing mechanical advantage during actuation.

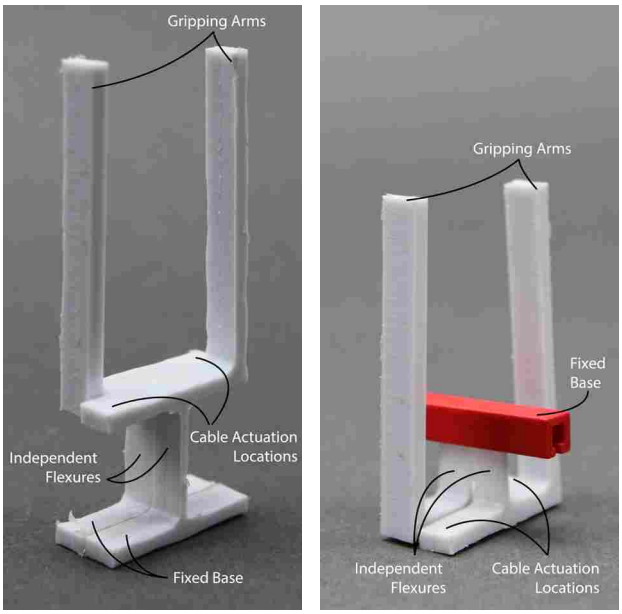

(a) (b)

Figure 3.1: (a) L-Arm and (b) Inverted L-Arm polypropylene prototypes.

These challenges are considered while exploring the geometry, strain-deflection relationship, and possible manufacturing methods for a 2-degree-of-freedom gripper compliant mechanism. A large-scale prototype with a 38 mm diameter shaft was created to demonstrate mechanism functionality. A 6 mm diameter prototype was also created. Finite element (FE) analysis was used to determine the strain-deflection relationship of the flexures for a 3 mm device. A fatigue analysis was carried out for the nitinol (hereafter referred to as NiTi) flexure material to determine feasibility.

Research has been conducted regarding the application of compliant mechanisms in minimally invasive surgery, including MIS wrist mechanisms. A review of wrist mechanisms is found in [47]. Compliant designs include a superelastic NiTi wrist [37], an asymmetric wrist [48], and a virtual center compliant MIS tool [49]. Compliant end-effector designs include an endoscopic suturing device [50], a statically balanced surgical grasper [51], a force-limiting scalpel [52], and the origami-inspired compliant forceps, the Oriceps [17].

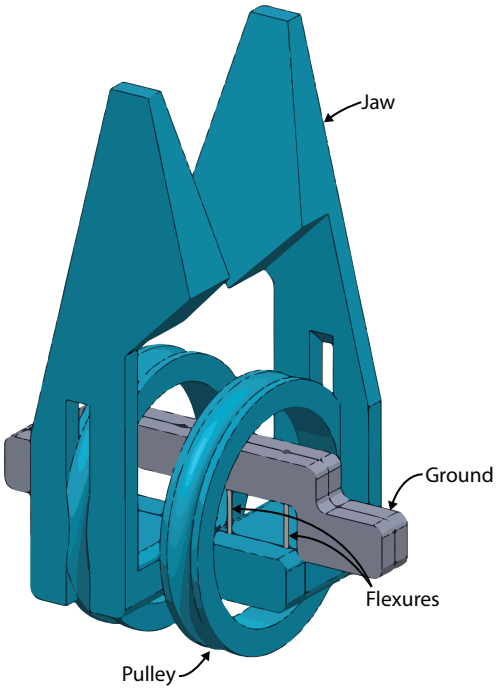

Figure 3.2: Inverted L-Arm with NiTi wire flexures. While both identical jaws are shown only one has been labeled.

3.2 Inverted L-Arm Concept

The L-Arm gripper mechanism concept was developed to demonstrate the feasibility of overcoming the three challenges in this context associated with compliant mechanisms noted earlier: inadequate performance in compression, high stresses induced while under large deformations, and a mechanical advantage that varies as a function of deflection. The flexure-based L-Arm gripper is a compliant mechanism composed of two opposing L-shaped grippers with flexures that enable each of the jaws to actuate independently as shown in Fig. 3.1a. The L-Arm gripper shows promise due to the simplicity of the mechanism and the possibility to increase performance over current mesoscale instruments, including larger deflections and additional degrees of freedom. A low part count and relatively large minimum feature size can be scaled to the millimeter size while maintaining function and performance.

The L-Arm has 2 degrees of freedom (DoF), one wrist and one gripping. The jaws pivot independently about the same axis of rotation. Figure 3.2 shows the L-Arm with one jaw labeled. The pulley and jaw are rigidly connected and can be made as one part. The flexure connects the jaw to the ground link (which is connected to the instrument shaft). The second jaw is identical to

the first and is rotated 180 degrees so the jaws face each other. A side view schematic of a single jaw is shown in Fig. 3.3. The moment arm for the cables is determined by the pulley radius, R. The approximate center of rotation is labeled CoR. F_1 and F_2 are each a combination of preload and actuation forces.

3.2.1 Addressing Compressive Loads

Most robotic minimally invasive surgical instrument designs locate the end-effector at the distal end of a long shaft. Cables extending the length of the shaft actuate the instrument and also induce a compressive preload on the system. Conventional compliant mechanisms often have low resistance to compressive loading and may buckle if the compressive load is too high. Inverting compliant mechanisms can enable them to support high compressive loads and has been studied previously [46]. This principle of inversion was applied to the L-Arm design as shown in Fig. 3.1b. The inversion of flexures in the L-Arm mechanism eliminates the occurrence buckling by placing the flexible members normally in compression in tension. Note that a load causing the flexures to be in compression in Fig. 3.1a would result in tensile loading of the flexures in Fig. 3.1b. In Fig. 3.1a the mechanism consists of, from bottom to top, a base or ground, flexures, and L-shaped jaws. As a downward actuation force is applied to either extreme of the horizontal segment of the L-shaped jaw, the respective flexure is placed in compression. In Fig. 3.1b the inverted mechanism consists of, from bottom to top, the L-shaped jaws, flexures, and red ground link. As a downward actuation force is applied to either extreme of the horizontal segment of the L-shaped jaw, the respective flexure is placed in tension. In this way the first challenge of inadequate performance in compression is overcome.

3.2.2 Addressing Stresses Due to Large Deformations

There are three fundamental ways to modify a flexure's stiffness (and therefore control stresses): geometry, boundary conditions, and material properties. These three ways can be varied independently to tailor a compliant flexure for a specific application.

While the large-scale proof-of-concept 38 mm L-Arm prototypes described in this paper (see Fig. 3.2) were created with flexures consisting of two wires placed side by side, it is expected

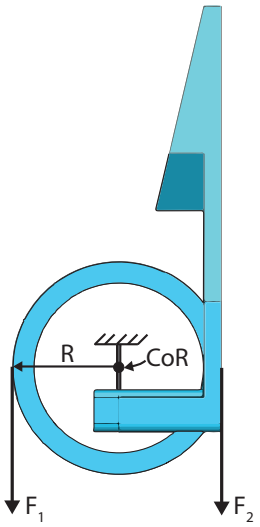

Figure 3.3: A single jaw of the L-Arm compliant mechanism viewed from the side. R is the moment arm length (radius of the pulley), CoR is the approximate center of rotation, and F_1 and F_2 are input forces provided by cables.

that the flexures in the 3 mm L-Arm design will have a rectangular cross-section. The following discussion on flexure geometry assumes a rectangular cross-section.

The L-Arm flexure geometry was designed to minimize bending stress while still providing adequate strength in tensile loading. To this end, the thickness of the flexures was decreased to enable higher angular deflection before reaching the limiting bending stress. The flexure width was kept as large as possible to provide lateral and torsional stability.

The flexible members of the L-Arm were designed using the pseudo-rigid-body model with the small-length flexural pivot (SLFP) assumption, which is that if the flexure length is small compared to the rigid portion of the mechanism the center of rotation of the mechanism can be approximated as the midpoint of the flexure along its length. The SLFP assumption is valid when the flexible member length, l, is much less than the overall length, L, of the mechanism ($l \ll L$). [29]

The SLFP assumption simplifies the kinematic analysis of the mechanism to that of a simple pin joint with rigid links. The jaw faces were designed such that the plane in which each face lies passes through the axis of rotation of the flexures. When in the closed position the jaw faces make complete contact with each other. Note that the compliant nature of the mechanism enables the contact profile of the jaws to be tailored for a specific task or procedure. The actuation pulleys were also designed with their axes of rotation aligned with those of their respective flexure.

The L-Arm flexure has boundary conditions where one side of the flexure is fixed to ground while the other side is fixed to the moving jaw. These boundary conditions are also part of the SLFP assumption.

Several materials were identified as possible candidates for the flexure including stainless steel, titanium, metallic glass, and the nickel titanium alloy nitinol (NiTi). These materials were selected for their favorable compliant characteristics, including a relatively large $\frac{S_y}{E}$, as well as biocompatibility [34, 35, 53]. NiTi consists of nearly equal atomic percentages of nickel and titanium. NiTi can exhibit the superelastic effect and is therefore of interest in the field of compliant mechanisms due to the large strains that it can undergo before yielding. It can reach strains of 6-8% with very small material set, while steels generally reach strains on the order of less than 1% before yielding.

Analysis determined that a stainless steel flexure could undergo angular deflections of $< 30^\circ$ for a given geometry before yielding. A metallic glass flexure was designed that could deflect to $\sim 45^\circ$ [20]. NiTi was investigated for its ability to undergo large strains before yielding and was ultimately chosen as the flexure material due to its potentially large range of motion.

A finite element model was created, as described in the FE Model section, to analyze the strain-deflection relationship of an NiTi flexure in bending. Superelastic NiTi is commercially available in form factors that include wire, rod, tubing, strip and sheet. A NiTi strip of 0.102 mm (the smallest thickness available) was used in the FE model, fatigue analysis, and in the construction of the 6 mm prototype.

The selection of superelastic NiTi as the flexure material overcame the second challenge and enabled the L-Arm mechanism to reach the large deflections required in MIS instruments.

3.2.3 Addressing Variable Mechanical Advantage

The third challenge encountered with early L-Arm concepts (see Fig. 3.1) was a variable actuation moment arm that tended to zero as the mechanism was deflected. Once the effective length of the actuation moment arm reached zero the L-Arm could not be deflected farther even if the flexure itself was designed for greater angular deflections.

To overcome this challenge a pulley was integrated into each gripper jaw to maintain a constant moment arm for the cables as the mechanism is actuated. The cable is fixed at the top

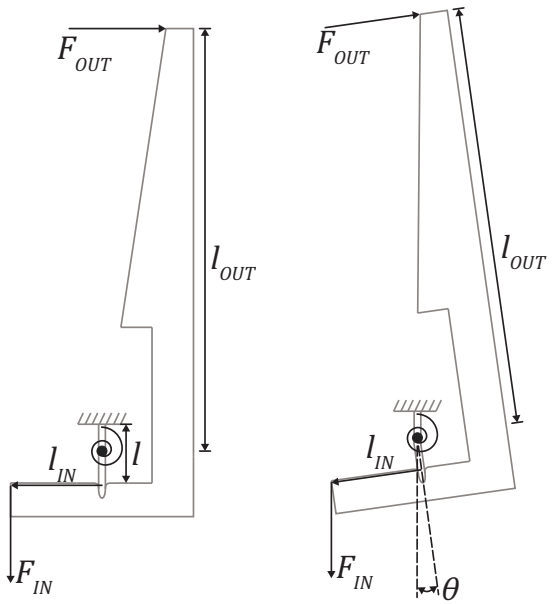

(a) (b)

Figure 3.4: Model used in the mechanical advantage analysis of the L-Arm gripper mechanism without a pulley. Note that F_{out} is modeled as a follower force while F_{in} is modeled as a vertical force. The location at which F_{in} is applied changes relative to the approximate center of rotation as the mechanism is actuated.

of the pulley and routed over each side. Figure 3.3 shows the pulley geometry. The forces F_1 and F_2 are transmitted from the back (proximal) end of the instrument to the L-Arm mechanism via the cables. The cables are placed in opposing pairs because they only transmit tensile forces. The pulley and jaw can be made as one piece, reducing the mechanism part count and simplifying the manufacturing process. The circular pulley was designed with its center at the mid-point of the flexure. Using the SLFP assumption this is also the approximate center of rotation of the jaw. While the resulting mechanical advantage is not constant, the variability is significantly reduced. The integrated pulley enables angular deflections exceeding $\pm 90^\circ$ for each jaw to be achieved using cable actuation.

A mechanical advantage analysis was completed to compare the L-Arm with and without the integrated pulley. A labeled diagram of one jaw of the L-Arm without a pulley used in the analysis is shown in Fig. 3.4. For the L-Arm without a pulley the mechanical advantage calculations are outlined as follows:

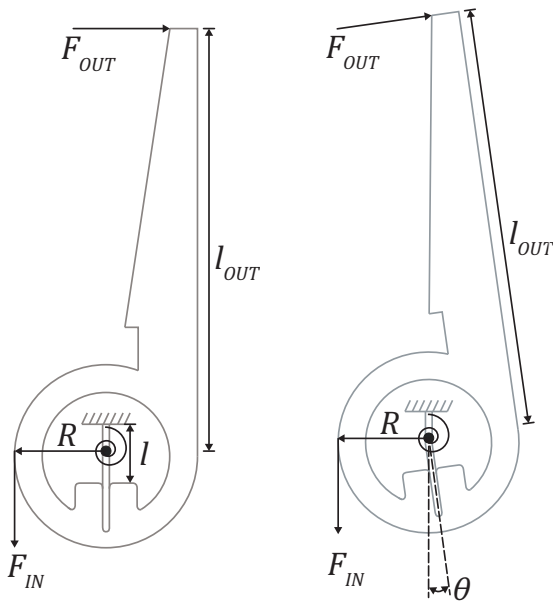

(a) (b)

Figure 3.5: Model used in the mechanical advantage analysis of the L-Arm gripper mechanism with a pulley integrated into the jaw. Note that F_{out} is modeled as a follower force while F_{in} is modeled as a vertical force. The location at which F_{in} is applied does not change relative to the approximate center of rotation as the mechanism is actuated.

The sum of the moments about the approximate center of rotation is

$$F_{in}\left(l_{in}\cos(\theta)-\frac{l}{2}\sin(\theta)\right)=T+F_{out}l_{out} \tag{3.1}$$

where F_{in} is the input force, l_{in} is the perpendicular distance from the flexure to the point at which the input force is applied (for this analysis l_{in} is equal to the radius of the pulley, R, used in the analysis of the L-Arm mechanism with an integrated pulley), θ is the angular deflection from the nominal (undeflected state), T is the torque due to the torsional spring at the center of the flexure, F_{out} is the output force at the tip of the jaw, and l_{out} is the perpendicular distance from center of rotation to the output force. Using the pseudo-rigid-body model the SFLP assumption the flexure is modeled as a pin joint with a torsional spring at the mid-length of the flexure. The torque, T, due to the torsional spring is defined as

$$T=\frac{EI}{l}\theta \tag{3.2}$$

where E is the modulus of elasticity of the flexure, I is the second moment of area, and l is the flexure length. Substituting equation 3.2 into equation 3.1 and solving for the mechanical advantage, $\frac{F_{out}}{F_{in}}$, results in the following

$$MA_{np} = \left(\frac{1}{l_{in}\cos(\theta) - \frac{l}{2}\sin(\theta)} \left(\frac{EI\theta}{F_{out}l} + l_{out} \right) \right)^{-1} \tag{3.3}$$

Where MA_{np} is the mechanical advantage of the L-Arm mechanism without the integrated pulley. The analysis of the L-Arm mechanism with integrated pulley is outlined below. Figure 3.5 shows the diagram of the L-Arm with a pulley used in the analysis. The sum of the torques about the approximate center of rotation is

$$F_{in}R = T + F_{out}l_{out} \tag{3.4}$$

Where R is the radius of the integrated pulley. Solving for the mechanical advantage, $\frac{F_{out}}{F_{in}}$, results in

$$MA_p = \left(\frac{T}{F_{out}R} + \frac{l_{out}}{R} \right)^{-1} \tag{3.5}$$

Where MA_p is the mechanical advantage of L-Arm mechanism with an integrated pulley. Substituting equation 3.2 into equation 3.5 results in the following:

$$MA_p = \left(\frac{EI\theta}{F_{out}Rl} + \frac{l_{out}}{R} \right)^{-1} \tag{3.6}$$

Using the values in Table 3.1, the mechanical advantage for the L-Arm with and without the integrated pulley was calculated as a function of angular deflection. Figure 3.6 shows the mechanical advantage for a 3 mm L-Arm with and without a pulley. Titanium was used for simplicity in the model. The material modulus of elasticity will only affect the shape of the curve, not the point at which the mechanical advantage becomes negative (for the L-Arm without a pulley). The point at which the curve crosses zero is dictated by the effective moment arm for the input force, F_{in}. The plot also shows that the mechanical advantage of the L-Arm design with a pulley has less variation compared to the L-Arm without a pulley and it never becomes negative. For the chosen geometry, the L-Arm without a pulley can be actuated via cables up to $\sim 65^{\circ}$ degrees before the

mechanical advantage reaches zero. The L-Arm design with a pulley can be cable-actuated over the desired range of motion, $\pm 90^{\circ}$. Although the mechanical advantage is much less than 1 for both designs it is not anticipated to be a problem for robotic MIS instruments driven by powerful electric motors that can develop the torques necessary to obtain the desired output force at the tip of the instrument. Current commercial instrument architectures have similar mechanical advantages as the L-Arm concept. In this case a 2 N output force was used as the working load for a 3 mm surgical instrument.

3.3 Large-Scale Proof-of-Concept Prototype

Multiple rounds of prototyping and mathematical modeling were used to verify that the strategies outlined in this work could enable feasible compliant mechanisms capable of the desired performance (2 DoF and an angular deflection $\pm 90^{\circ}$, as well as the ability to perform gripping and lifting functions). A large-scale proof-of-concept prototype was constructed to test the inverted L-Arm concept. The jaws and ground link were made of PLA using an additive manufacturing process. The actuation cables were made using 0.84 mm polyester twine. The shaft tube was a 38 mm clear cellulose tube. The flexures were made using 0.38 mm (0.015 in) diameter superelastic NiTi wire. The flexures are ~ 5 mm in length. Two wires were placed side-by-side at a distance of 5 mm to create the flexure for each jaw. The torsional stiffness (about an axis parallel to the instrument shaft axis) of the jaws is increased by moving the two NiTi wires apart from each other. The prototype is shown in Figs. 3.7 and 3.8.

Table 3.1: Values used in mechanical advantage analysis of a 3 mm L-Arm mechanism.

dimension	value
l	1.25 mm
h	0.102 mm
b	0.7 mm
l_{in}	1.299 mm
l_{out}	7.0 mm
R	1.299 mm
E	113.8 GPa
F_{out}	2.0 N

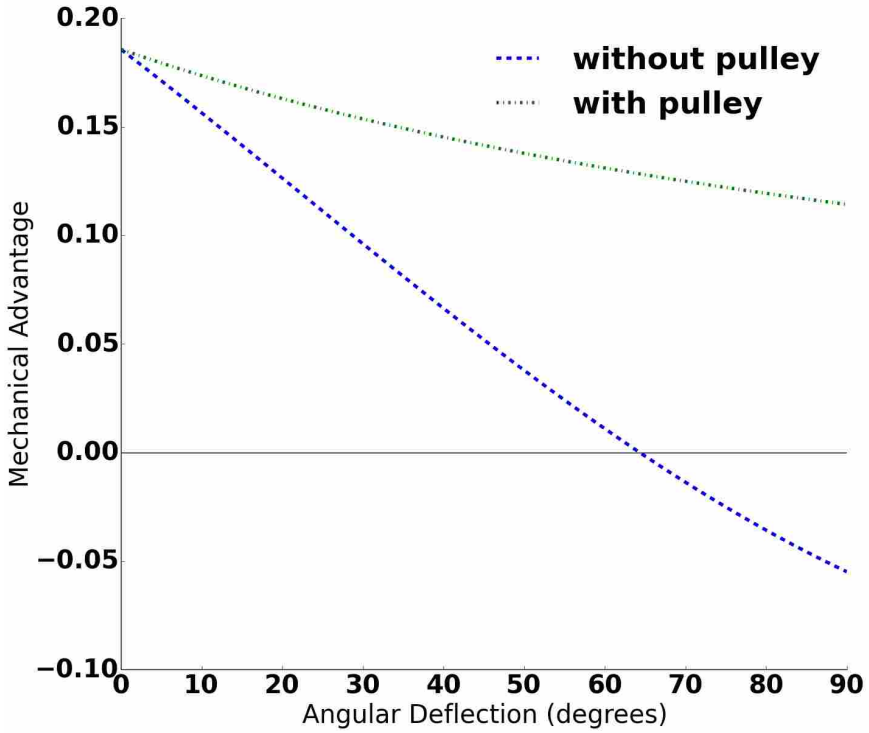

Figure 3.6: Mechanical advantage plotted against angular deflection (in degrees) for a 3 mm L-Arm using the values listed in Table 3.1.

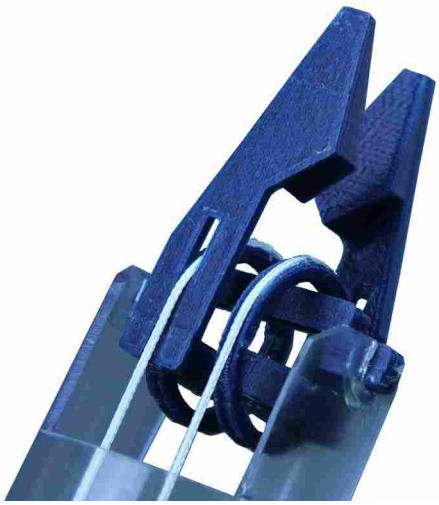

Figure 3.7: 38 mm proof-of-concept prototype of the inverted L-Arm with NiTi wire flexures.

The jaws are independently actuated via the cables. The prototype was able to undergo $\pm 90^\circ$ from the undeflected position without yielding, and demonstrated the ability to perform

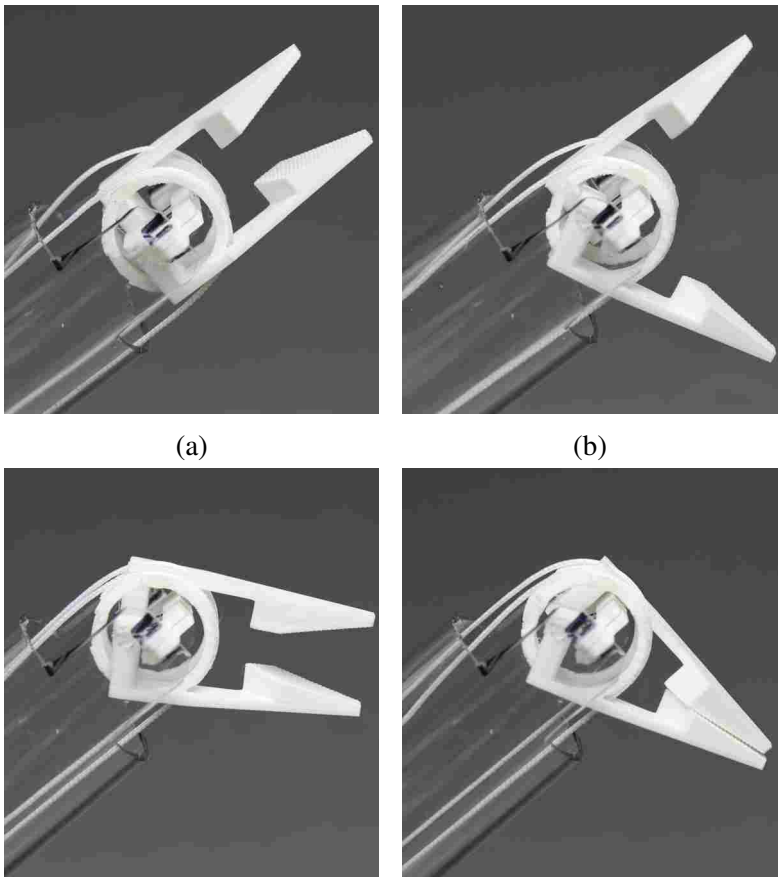

(a) (b)

(c) (d)

Figure 3.8: 38 mm L-Arm prototype showing independent actuation of each jaw as well as the gripping function of the mechanism.

gripping and lifting functions. The lifting function consisted of gripping an object, lifting it, and moving it to a new location supported by only the gripper mechanism.

3.4 3 mm and 6 mm L-Arm Designs

Preliminary finite element analysis was done for a 3 mm L-Arm mechanism flexure. 3 mm and 6 mm mechanisms were also modeled (see Fig. 3.9). Jaws and ground links for 3 mm and 6 mm prototypes were made using a stereolithography (SLA) additive manufacturing process. The 6 mm parts were assembled with NiTi flexures to create a 6 mm prototype.

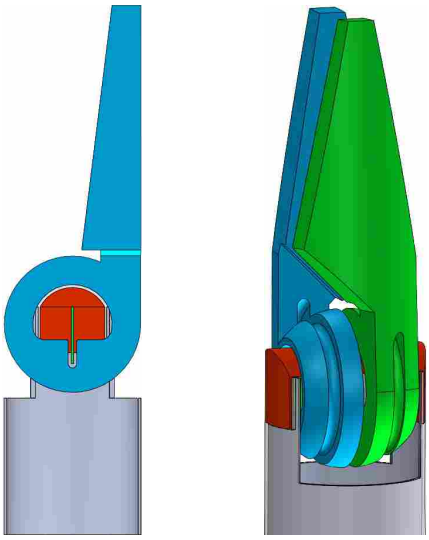

(a) (b)

Figure 3.9: 6 mm L-Arm model. (a) shows a section view with the jaw shown in blue, the NiTi flexure in green, and the fixed portion in red. (b) is a model of the assembled mechanism.

3.4.1 FE Model

A finite element model of a 3 mm L-Arm flexure was created using ANSYS 15.0 and SOLID186 elements. A 1.25 mm flexure with a larger moment arm (about 12.5 mm long) was modeled. A schematic of the FE model is shown in Fig. 3.10. The moment arm was modeled such that it is rigid in comparison to the flexure. A follower force was applied to the end of the moment arm to deflect the flexure. The mesh was refined in the flexure volume and approximately 30,000 elements were used. The *Shape Memory* material model was implemented using the values found in Liu et al. (see Table 3.3) where E is the modulus of elasticity of the austenite phase, μ is Poisson's ratio, σ_s^{AS} is the starting stress value of the forward phase transformation, σ_f^{AS} is the final stress value of the forward phase transformation, σ_s^{SA} is the starting stress value of the reverse phase transformation, σ_f^{SA} is the final stress value of the reverse phase transformation, $\overline{\varepsilon}_L$ is the maximum residual strain, and α is the material response ratio between tension and compression [37].

Based on these results, a NiTi flexure with dimensions found in Table 3.2 is predicted to undergo angular deflections over $\sim 90^\circ$ before yielding occurs. Figure 3.11 shows the flexure deflected to $\sim 88.6^\circ$ with a total von Mises strain of 6.3%. For this strain level the flexure has

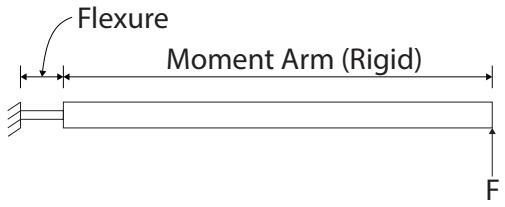

Figure 3.10: Schematic of the boundary conditions and geometry used in the FE model. The flexure is fixed on the left side and a follower force, F, is applied to the moment arm on the right side.

an expected fatigue life of approximately 1,000 cycles [41]. Fatigue life must be considered in the design and implementation of surgical instrument to prevent failure during use.

3.4.2 3 mm and 6 mm Prototypes

Parts for a 3 mm prototype were created using an SLA process. One jaw of the 3 mm L-Arm is shown in Fig. 3.12. A more robust 6 mm SLA prototype was also created (see Figs. 3.13 and 3.14). These prototypes demonstrate that the minimum feature size of the 3 mm and 6 mm designs can be achieved with current commercial technologies. The 6 mm prototype also verified that the design was able to be assembled.

3.4.3 Fatigue Testing

Minimally invasive surgical instruments must undergo many cycles during a given procedure. As a rule of thumb, instruments should be designed for up to 1,000 cycles per procedure. Note that this value is dependent on the particular procedure and other clinical considerations and is therefore only used as starting point. Fatigue testing of superelastic NiTi has been studied previously [54–56]. The NiTi material used to create the 6 mm prototype flexures was tested to determine fatigue life to verify that it could be useful for use in MIS instruments. The flexure

Table 3.2: NiTi flexure dimensions used in the 3 mm FE model.

	dimension, mm
flexure length	1.25
flexure thickness	0.102
flexure width	0.25

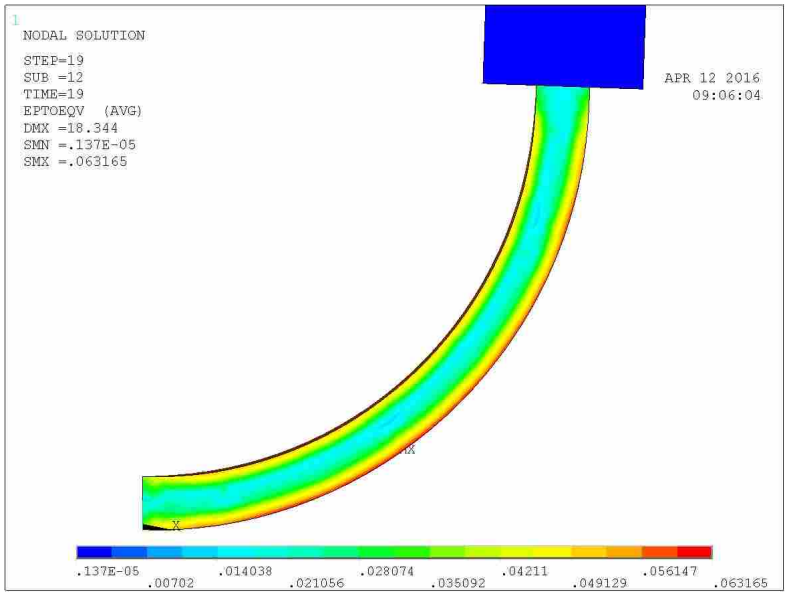

(a)

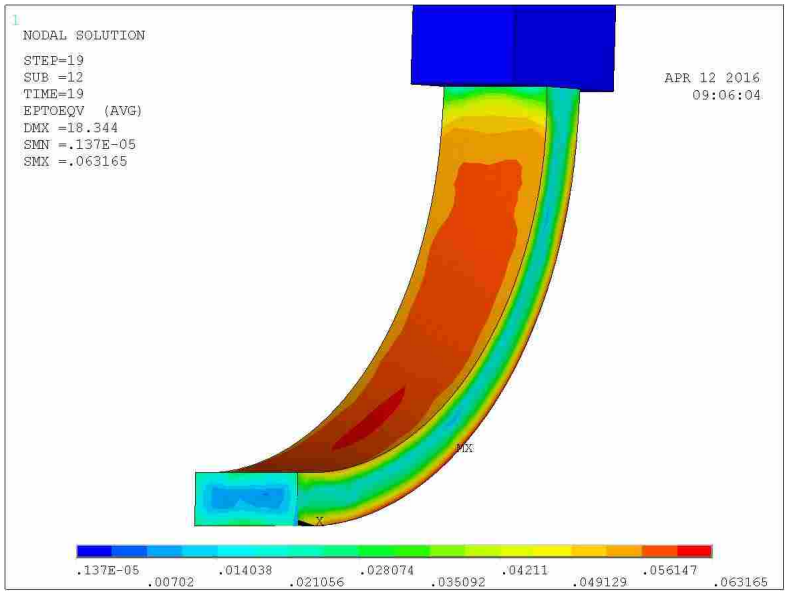

(b)

Figure 3.11: FE model of a flexure with NiTi nonlinear material properties. Flexure dimensions are for a 3 mm instrument as listed in Table 3.2. The total von Mises strain is plotted.

geometry as tested is listed in Table 3.4. Flexures of two lengths, 1.25 mm and 3 mm, were tested. These material dimensions were used as a starting point to verify that NiTi is a viable material for use as a flexure in a compliant gripper mechanism. Figure 3.15 shows the fatigue fixture used to test the flexures. The fixture accommodated testing of up to six flexures simultaneously. A micro-controller monitored the number of cycles the flexures underwent as well as the continuity of each

Figure 3.12: 3 mm L-Arm SLA jaw (with support material) shown next to a US Penny for scale.

Figure 3.13: 6 mm L-Arm SLA parts shown in the as-manufactured state, including support material.

flexure. The number of cycles at which a given flexure lost continuity was recorded (indicating that the flexure had failed). The test ended when all flexures had failed. The flexures were deflected to 45° with fixed-guided boundary conditions. These results (see Table 3.5) show that NiTi is a viable flexure material and could be used in MIS instruments. For the geometric constraints of the end effector, NiTi can undergo many cycles before failure as would be required for a surgical instrument.

Table 3.3: Superelastic NiTi material properties used in the FE model.

Property	Value
E	44.0 GPa
μ	0.3
σ_s^{AS}	440 MPa
σ_f^{AS}	472 MPa
σ_s^{SA}	218 MPa
σ_f^{SA}	206 MPa
$\bar{\varepsilon}_L$	0.045
α	0

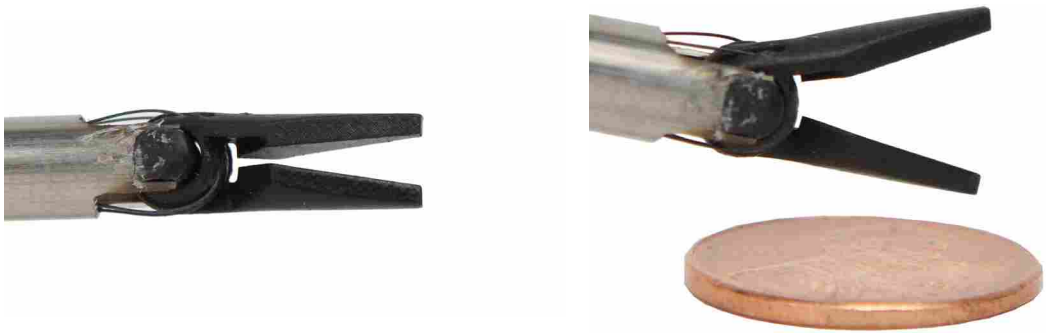

(a) (b)

Figure 3.14: 6 mm L-Arm SLA prototype with NiTi flexures. (a) shows the nominal state. (b) shows one jaw in a deflected state. US penny for scale.

Note that Table 3.5 contains the data with outliers removed. The flexure in the left-most position of the fatigue fixture (as seen in Fig. 3.15) consistently failed much earlier than the other flexures. This resulted in a large standard deviation in the experimental data and could be due to the tolerances of the fixture itself. If these outliers are included in the data the mean becomes 2,130 and 9,944 cycles and the standard deviations are 586 and 3,459 for the 1.25 mm and 3 mm flexures, respectively. These fatigue data give a starting point for specifying the number of cycles and procedures an instrument of a particular geometry could undergo before being retired from use.

Table 3.4: NiTi flexure dimensions used in fatigue testing.
Flexures of two lengths were tested.

	dimension, mm (in)
flexure length	1.25, 3.00 (0.049, 0.118)
flexure thickness	0.102 (0.004)
flexure width	2.032 (0.08)

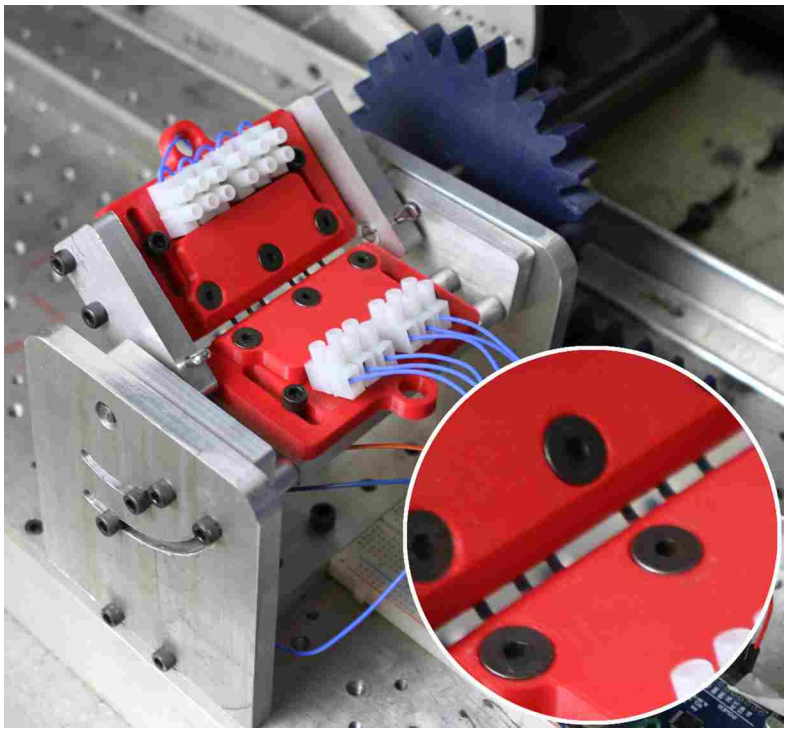

Figure 3.15: Fatigue fixture for testing NiTi flexures. The 6 flexures being tested can be seen in the gap between the two red fixture plates (see inset).

Table 3.5: Fatigue test results for 1.25 mm and 3 mm NiTi flexures. The mean and standard deviation for flexure length are reported. The flexures were displacement loaded to an angle of 45°. Note that this data excludes an outlier in each of the trials as explained in the text.

flexure length, mm	Mean (cycles)	Standard Deviation
1.25	2,369	265
3.00	11,420	1,138

3.5 Conclusion

This work addressed the three challenges of employing compliant mechanisms as grippers in cable-actuated minimally invasive surgery instruments: compressive loading, maximum angular deflection, and a variable actuation moment arm. These issues were resolved by inverting the mechanism, designing appropriate geometry and boundary conditions, employing NiTi flexures, and integrating a pulley into each jaw. The angular rotation is predicted to be at least $\pm 90^\circ$.

Fatigue analysis shows that a 3 mm NiTi flexure should undergo over 10,000 cycles before failure while a 1.25 mm NiTi flexure is expected to be cycled over 2,000 times before failure when displaced to an angle of 45°. These results are promising and show that the NiTi flexures can not only be deflected to a 90°, but can also be cycled many times before failure.

The 3 mm L-Arm concept as designed has a total of six parts, four of which are unique. A lower part count compared to commercially available instruments could reduce cost and improve the availability of MIS procedures for a broad range of patients [22].

The inverted L-Arm compliant mechanism is a good candidate for a 3 mm 2 DoF minimally invasive surgical instrument. A third degree of freedom could be added by locating an existing 1 DoF wrist mechanism with an axis of rotation orthogonal to the axis of rotation of the L-Arm below the end-effector.

The principles and strategies developed here may prove useful in creating other compliant mechanism surgical instruments.

CHAPTER 4. CONCLUSION

This work is the result of an effort to develop smaller, higher-performance minimally invasive surgical instruments. The use of compliant mechanisms can eliminate frictional forces, reduce part count, and increase manufacturability. The constraints of MIS were used to guide this research and push the boundaries of compliant mechanisms.

Two compliant mechanism designs were realized that have potential to be integrated into commercial surgical instruments. Models were created to aid in their design. The parametrized finite element models for the CCAFP and L-Arm gripper flexures have been included in appendices A and B for reference. The CCAFP concept was prototyped at the 3 mm size and shown to preform as predicted. Further development shows promise for a 2 DoF CCAFP design with intersecting axes of rotation resulting in a low swept volume and potential increase in performance over stacked wrist mechanisms. The L-Arm was prototyped at 6 mm (also a viable instrument size) and modeling shows the potential to scale to 3 mm. Three challenges associated with compliant mechanisms in MIS applications: compressive forces, high bending stress, and highly-variable mechanical advantage were respectively resolved using the technique of inversion, tailoring flexure geometry and selection of nitinol, and the addition of integrated pulleys.

Nitinol was considered as a candidate material for use in compliant surgical devices due to its unique superelastic characteristics and excellent biocompatibility. Nitinol was proposed for use in both the CCAFP and L-Arm gripper mechanisms due to its potential for large deformations. A fatigue test was done for a simple flexure with a rectangular cross section that shows promise for the use of nitinol in MIS instruments. Although nitinol has nonlinear material properties, the displacement loading of the instruments should not be affected.

Based on the results of this research, compliant mechanisms are shown to be a viable alternative to traditional methods of achieving motion used in minimally invasive surgical instrument designs. The use of compliant mechanisms could enable a reduction in instrument size while main-

taining a large range of motion. While the design constraints limit the compliant flexures to small sizes, the use of nitinol enables large deflections. Although the integration of stress-limiting cam surfaces did not improve the performance of the 3 mm CCAFP, they could be useful for certain compliant mechanism designs. The principles and models outlined in this work could be employed by others in the design of compliant mechanisms for surgical instruments and other applications.

REFERENCES

[1] Metzelder, M., and Ure, B., 2010. "[minimally invasive pediatric surgery].." *Der Chirurg; Zeitschrift fur alle Gebiete der operativen Medizen,* **81**(1), pp. 71–80. 1

[2] Ullrich, F., Bergeles, C., Pokki, J., Ergeneman, O., Erni, S., Chatzipirpiridis, G., Pané, S., Framme, C., and Nelson, B. J., 2013. "Mobility experiments with microrobots for minimally invasive intraocular surgerymicrorobot experiments for intraocular surgery." *Investigative ophthalmology & visual science,* **54**(4), pp. 2853–2863. 1

[3] Miyamoto, H., Leechavengvongs, S., Atik, T., Facca, S., and Liverneaux, P., 2014. "Nerve transfer to the deltoid muscle using the nerve to the long head of the triceps with the da vinci robot: six cases." *Journal of reconstructive microsurgery,* **30**(06), pp. 375–380. 1

[4] Mack, M. J., 2001. "Minimally invasive and robotic surgery." *Jama,* **285**(5), pp. 568–572. 2, 3

[5] Krpata, D. M., and Ponsky, T. A., 2013. "Needlescopic surgery: whats in the toolbox?." *Surgical endoscopy,* **27**(3), pp. 1040–1044. 3

[6] Vitiello, V., Lee, S.-L., Cundy, T. P., and Yang, G.-Z., 2013. "Emerging robotic platforms for minimally invasive surgery." *Biomedical Engineering, IEEE Reviews in,* **6**, pp. 111–126. 3

[7] Ma, R., Wu, D., Yan, Z., Du, Z., and Li, G., 2010. "Research and development of micro-instrument for laparoscopic minimally invasive surgical robotic system." In *Robotics and Biomimetics (ROBIO), 2010 IEEE International Conference on*, IEEE, pp. 1223–1228. 3

[8] Saedi, S., Mirbagheri, A., and Farahmand, F., 2011. "Conceptual design of a miniaturized hybrid local actuator for minimally invasive robotic surgery (mirs) instruments." In *Engineering in Medicine and Biology Society, EMBC, 2011 Annual International Conference of the IEEE*, IEEE, pp. 2140–2143 Piezo electric actuation near the end of the instrument. 3

[9] Minor, M., and Mukherjee, R., 1999. "A dexterous manipulator for minimally invasive surgery." In *Robotics and Automation, 1999. Proceedings. 1999 IEEE International Conference on*, Vol. 3, IEEE, pp. 2057–2064. 3

[10] Wallace, D., Rosa, D., and Moll, F., 2001. Surgical instrument with extended reach for use in minimally invasive surgery, Nov. 6 US Patent 6,312,435. 3

[11] Van Meer, F., Giraud, A., Esteve, D., and Dollat, X., 2005. "A disposable plastic compact wrist for smart minimally invasive surgical tools." In *Intelligent Robots and Systems, 2005.(IROS 2005). 2005 IEEE/RSJ International Conference on*, IEEE, pp. 919–924. 3

[12] Jelínek, F., Pessers, R., and Breedveld, P., 2014. "Dragonflex smart steerable laparoscopic instrument." *Journal of Medical Devices,* **8**(1), p. 015001. 3

[13] http://www.intuitivesurgical.com/, 2015. 3

[14] Shang, J., Noonan, D. P., Payne, C., Clark, J., Sodergren, M. H., Darzi, A., and Yang, G.-Z., 2011. "An articulated universal joint based flexible access robot for minimally invasive surgery." In *Robotics and Automation (ICRA), 2011 IEEE International Conference on*, IEEE, pp. 1147–1152 This is not a robotic instrument, but does have 7 DOF. 3

[15] Lee, C., Park, W. J., Kim, M., Noh, S., Yoon, C., Lee, C., Kim, Y., Kim, H. H., Kim, H. C., and Kim, S., 2014. "Pneumatic-type surgical robot end-effector for laparoscopic surgical-operation-by-wire." *Biomedical engineering online,* **13**(1), p. 130. 3

[16] Zoppi, M., Sieklicki, W., and Molfino, R., 2008. "Design of a microrobotic wrist for needle laparoscopic surgery." *Journal of Mechanical Design,* **130**(10), p. 102306. 3

[17] Edmondson, B. J., Bowen, L. A., Grames, C. L., Magleby, S. P., Howell, L. L., and Bateman, T. C., 2013. "Oriceps: Origami-inspired forceps." In *ASME 2013 Conference on Smart Materials, Adaptive Structures and Intelligent Systems*, American Society of Mechanical Engineers, pp. V001T01A027–V001T01A027. 3, 6, 30

[18] Frecker, M. I., Powell, K. M., and Haluck, R., 2005. "Design of a multifunctional compliant instrument for minimally invasive surgery." *Journal of biomechanical engineering,* **127**(6), pp. 990–993. 3, 6

[19] Tanner, J. D., Grames, C., Jensen, B. D., Magleby, S. P., and Howell, L. L., 2015. "Millimeter-scale robotic mechanisms using carbon nanotube composite structures." *Journal of Mechanisms & Robotics,* **7**(2) paper 021001 (7 pages), DOI: 10.1115/1.4029436. 3, 5

[20] Tanner, J. D., 2014. "Design and analysis of robotically-controlled minimally invasive surgical instruments." Master's thesis, Brigham Young University, Provo, Utah. 5, 34

[21] Grames, C. M., 2015. "Design and manufacture of mesoscale robot-actuated surgical instruments." Master's thesis, Brigham Young University, Provo, Utah. 5

[22] Grames, C. L., Tanner, J. D., Jensen, B. D., Magleby, S. P., Steger, J. R., and Howell, L. L., 2015. "A meso-scale rolling-contact gripping mechanism for robotic surgery." In *ASME 2015 International Design Engineering Technical Conferences and Computers and Information in Engineering Conference*, American Society of Mechanical Engineers, pp. V05AT08A034–V05AT08A034. 5, 47

[23] Weinstein, W. D., 1965. "Flexure-pivot bearings. i-spring rate, bearing types, single-strip design(flexure-pivot bearing types, spring rate and single strip design useful for limited angular movement)." *Machine Design,* **37**, pp. 150–157. 6

[24] Wittrick, W., 1951. "The properties of crossed flexure pivots, and the influence of the point at which the strips cross." *Aeronautical Quarterly,* **2**(4), pp. 272–292. 6

[25] Jensen, B. D., and Howell, L. L., 2002. "The modeling of cross-axis flexural pivots." *Mechanism and machine theory,* **37**(5), pp. 461–476. 6, 8, 13, 25

[26] Hongzhe, Z., Shusheng, B., Jingjun, Y., and Jun, G., 2012. "Design of a family of ultra-precision linear motion mechanisms." *Journal of Mechanisms and Robotics,* **4**(4), p. 041012. 6

[27] Merriam, E., Jones, J., Magleby, S., and Howell, L., 2013. "Monolithic 2 dof fully compliant space pointing mechanism." *Mechanical Sciences,* **4**, pp. 381–390. 6

[28] Stratton, E. M., 2014. Cross-flexural pivot, Apr. 29 US Patent 8,708,593. 6, 27

[29] Howell, L. L., 2001. *Compliant mechanisms*. John Wiley & Sons. 6, 29, 33

[30] Nai, T. Y., Herder, J. L., and Tuijthof, G. J., 2011. "Steerable mechanical joint for high load transmission in minimally invasive instruments." *Journal of Medical Devices,* **5**(3), p. 034503. 6

[31] Kota, S., Lu, K.-J., Kreiner, Z., Trease, B., Arenas, J., and Geiger, J., 2005. "Design and application of compliant mechanisms for surgical tools." *Journal of biomechanical engineering,* **127**(6), pp. 981–989. 6

[32] Aguirre, M. E., and Frecker, M., 2008. "Design innovation size and shape optimization of a 1.0 mm multifunctional forceps-scissors surgical instrument." *Journal of Medical Devices,* **2**(1), p. 015001. 6

[33] Duerig, T., Pelton, A., and Stöckel, D., 1999. "An overview of nitinol medical applications." *Materials Science and Engineering: A,* **273**, pp. 149–160. 7

[34] Haider, W., and Munroe, N., 2011. "Assessment of corrosion resistance and metal ion leaching of nitinol alloys." *Journal of materials engineering and performance,* **20**(4-5), pp. 812–815. 7, 34

[35] Ryhänen, J., Niemi, E., Serlo, W., Niemelä, E., Sandvik, P., Pernu, H., and Salo, T., 1997. "Biocompatibility of nickel-titanium shape memory metal and its corrosion behavior in human cell cultures." *Journal of biomedical materials research,* **35**(4), pp. 451–457. 7, 34

[36] Sieklicki, W., Zoppi, M., and Molfino, R., 2009. "Superelastic compliant mechanisms for needlescopic surgical wrists." In *Reconfigurable Mechanisms and Robots, 2009. ReMAR 2009. ASME/IFToMM International Conference on*, IEEE, pp. 392–399 Talks about superelastic NiTiNOL. 7

[37] Liu, J., Hall, B., Frecker, M., and Reutzel, E. W., 2013. "Compliant articulation structure using superelastic nitinol." *Smart Materials and Structures,* **22**(9), p. 094018. 7, 30, 41

[38] Cannon, J. R., Lusk, C. P., and Howell, L. L., 2005. "Compliant rolling-contact element mechanisms." In *ASME 2005 International Design Engineering Technical Conferences and Computers and Information in Engineering Conference*, American Society of Mechanical Engineers, pp. 3–13. 11

[39] Moon, Y.-M., 2007. "Bio-mimetic design of finger mechanism with contact aided compliant mechanism." *Mechanism and Machine Theory,* **42**(5), pp. 600–611. 13

[40] Otsuka, K., and Wayman, C., 1998. "Mechanism of shape memory effect and superelasticity." *Shape memory materials*, pp. 27–49. 17

[41] Nitinol technical properties http://jmmedical.com/resources/221/Nitinol-Technical-Properties.html, mar 2016. 17, 42

[42] Buselli, E., Valdastri, P., Quirini, M., Menciassi, A., and Dario, P., 2009. "Superelastic leg design optimization for an endoscopic capsule with active locomotion." *Smart materials and structures,* **18**(1), p. 015001. 18

[43] Howell, L., Magleby, S., and Olsen, B., 2013. *Handbook of Compliant Mechanisms*. Wiley. 25

[44] Drexel, M., Selvaduray, G., and Pelton, A., 2007. "The effects of cold work and heat treatment on the properties of nitinol wire." In *ASME 2007 2nd Frontiers in Biomedical Devices Conference*, American Society of Mechanical Engineers, pp. 89–90. 26

[45] Antoniou, S. A., Antoniou, G. A., Antoniou, A. I., and Granderath, F.-A., 2015. "Past, present, and future of minimally invasive abdominal surgery." *JSLS: Journal of the Society of Laparoendoscopic Surgeons,* **19**(3). 29

[46] Guérinot, A. E., Magleby, S. P., Howell, L. L., and Todd, R. H., 2005. "Compliant joint design principles for high compressive load situations." *Journal of Mechanical Design,* **127**(4), pp. 774–781. 29, 32

[47] Jelínek, F., Arkenbout, E. A., Henselmans, P. W., Pessers, R., and Breedveld, P., 2015. "Classification of joints used in steerable instruments for minimally invasive surgerya review of the state of the art." *Journal of Medical Devices,* **9**(1), p. 010801. 30

[48] York, P. A., Swaney, P. J., Gilbert, H. B., and Webster III, R. J., 2015. "A wrist for needle-sized surgical robots." In *Robotics and Automation (ICRA), 2015 IEEE International Conference on*, IEEE, pp. 1776–1781 This paper cites Liu et al. (Compliant articulation structure using superelastic NiTiNOL. 30

[49] Awtar, S., Trutna, T. T., Nielsen, J. M., Abani, R., and Geiger, J., 2010. "Flexdex: A minimally invasive surgical tool with enhanced dexterity and intuitive control." *Journal of Medical Devices,* **4**(3), p. 035003. 30

[50] Cronin, J. A., Frecker, M. I., and Mathew, A., 2008. "Design of a compliant endoscopic suturing instrument." *Journal of Medical Devices,* **2**(2), p. 025002. 30

[51] Aguirre, M., Steinórsson, Á. T., Horeman, T., and Herder, J., 2015. "Technology demonstrator for compliant statically balanced surgical graspers." *Journal of Medical Devices,* **9**(2), p. 020926. 30

[52] Bhargav, S. D., Chakravarthy, S., and Ananthasuresh, G., 2012. "A compliant end-effector to passively limit the force in tele-operated tissue-cutting." *Journal of Medical Devices,* **6**(4), p. 041005. 30

[53] Calin, M., Gebert, A., Ghinea, A. C., Gostin, P. F., Abdi, S., Mickel, C., and Eckert, J., 2013. "Designing biocompatible ti-based metallic glasses for implant applications." *Materials Science and Engineering: C,* **33**(2), pp. 875–883. 34

[54] Robertson, S., Pelton, A., and Ritchie, R., 2012. "Mechanical fatigue and fracture of nitinol." *International Materials Reviews,* **57**(1), pp. 1–37. 42

[55] Pelton, A., 2011. "Nitinol fatigue: a review of microstructures and mechanisms." *Journal of Materials Engineering and Performance,* **20**(4-5), pp. 613–617. 42

[56] McKelvey, A., and Ritchie, R., 2001. "Fatigue-crack growth behavior in the superelastic and shape-memory alloy nitinol." *Metallurgical and Materials Transactions A,* **32**(3), pp. 731–743. 42

APPENDIX A. CCAFP FINITE ELEMENT CODE

This appendix contains the finite element code used in the force-deflection and strain-deflection analysis of the cylindrical cross-axis flexural pivot (CCAFP). The code was written in the ANSYS Parametric Design Language (APDL) and run using a research licence of ANSYS 15.0. The CCAFP model is parametric to enable its analysis at arbitrary sizes. The model is pseudo-moment loaded using either a pressure on a small area at a distance from the approximate center of rotation or a couple applied in a similar manner. Both linear and nonlinear material models are implemented in the code; switching between them simply involves commenting and un-commenting the appropriate lines in the code. The nonlinear material model is used to analyze superelastic characteristics of the nickel-titanium alloy, nitinol. Time-history post-processing has been configured so that the relevant stress, strain, and deflection values are saved for each load step. These values, along with the model parameters, are exported and saved in two .csv files for further analysis.

```
!!!!!!!!!!!!!!!!!!!!!!!!!!!!!!!!!!!!!!!!!!!!!!!!!!!!!!!!!!!!!!!!!!!!!!!
!!!!!!!!!!!!!!!!!!!!!!!!!!!!!!!!!!!!!!!!!!!!!!!!!!!!!!!!!!!!!!!!!!!!!!!
!author: jason dearden
!email: byujason@gmail.com
!date: 30 december 2015

!compliant mechanisms research group
!department of mechanical engineering
!brigham young university
!provo, ut 84602

!description:
!this ansys batch file was written to run with ANSYS 15.0.
!it is a parametric FE model of a cylindrical cross-axis flexural
!pivot (CCAFP). this file includes the preprocessor, solver, and
!postprocessing code. there are two file outputs, one is a parameter
!file that contains parameters associated with the model, the other
!is a file containing stress, strain, and several points located on
!the CCAFP. both files are read into a companion python script that
!parses the data and outputs plots.

!NOTE: this batch file cannot be read in entirely. there are several
!code chunks that need to be left out, and others that are optional.


!!!!!!!!!!!!!!!!!!!!!!!!!!!!!!!!!!!!!!!!!!!!!!!!!!!!!!!!!!!!!!!!!!!!!!!
!!!!!!!!!!!!!!!!!!!!!!!!!!!!!!!!!!!!!!!!!!!!!!!!!!!!!!!!!!!!!!!!!!!!!!!



FINISH
!clear everything before starting running this batch file
/CLEAR

!change working directory to the local desktop -- ANSYS runs way faster if all files are local
/CWD,'C:\Users\dartsum\Desktop'
!change the jobname to something that makes sense. if the jobname is changed here it will
!also need to changed in the timehistory postprocessor code
jobname = 'ccafp_ansys'
/FILNAME,jobname,0
FINISH

!preprocessor -- this is where the parametric model is created and loads are applied
/PREP7
    !element type -- 20 node solid element. to use the SMA material model
    ET,1,SOLID186

    !material 1 properties
    !defines the temperature table -- in this case we are looking only at only temperature
    (room temperature)
    MPTEMP,1,0

    !steel
    !MPDATA,EX,1,,200e9
    !polypropylene -- note that it is 10^3 -- this is because we are using mm (this value is in
    MPa and the stress out will be in MPa)
```

```
!MPDATA,EX,1,,2e3
!MPDATA,PRXY,1,,0.45
!steel 304 is 193e3 MPa

!nitinol modulus of elasticity and poisson's ratio for the austenite phase
!modulus of elasticity

!value for tubes used in Liu, et al
!MPDATA,EX,1,,44e3 !MPa

!value from the literature
MPDATA,EX,1,,27.575e3 !MPa
!poisson's ratio
MPDATA,PRXY,1,,0.3

!shape memory material properties of NiTiNOL taken from the NDC values tabulated in
"Compliant Articulation
!Structure Using Superelastic NiTiNOL" Jiening Liu, Benjamin Hall, Mary Frecker and Edward
W Reutzel.
!Smart Materials and Structures 22 (2013) 094018 (11pp)

!TB,Lab,MAT,NTEMP,NPTS,TBOPT where the label is SMA, the material number is 1, the number
of temperatures
!to define variables for is 1, the number of datapoints to define for each temperature is
6, and SUPE is the
!Superelastic model (MEFF is the memory-effect model)

!TB,SMA,1,1,6,SUPE

!the temperature at which the TBDATA material properties are valid

!TBTEMP,-2.0

!6 parameters that define the superelastic stress strain relationship (with hysteresis)
!TBDATA,,C1,C2,C3,C4,C5,C6 where
!C1 is the starting stress value for the forward phase transformation,
!C2 is the final stress value for the forward phase transformation,
!C3 is the starting stress value for the reverse phase transformation,
!C4 is the final stress value for the reverse phase transformation,
!C5 is the maximum residual strain
!C6 is the parameter measuring the difference between material responses in tension and
compression

!values for tubes used in Liu, et al
!TBDATA,,440,472,218,206,0.045,0

!values from the literature
!TBDATA,,339,440.95,185.5,112.6,0.048,0



!model parameters
!easy way to define pi
pi = acos(-1)
!flexure angle -- 45 degrees -- changing the flexure angle is not yet supported. This value
!is used to calculate the flexure length only.
```

```
beta = pi/4

!instrument size -- use this to select between a 3mm, 5mm, and 8mm diameter ccafp
!the parameters can be changed (diameters and wall thicknesses of the cylinders)
ccafp_diameter = 3

!!!!!!!!!!!!!!!!!!!!!!!!!!!!!!!!!!!!!!!!!!!!!!!!!!!!!!!!!!!!!!!!!!!!!!!!!!!!!!!
!!!!!!!!!!!!!!!!!!!!!!!!!!!!!!!!!!!!!!!!!!!!!!!!!!!!!!!!!!!!!!!!!!!!!!!!!!!!!!!
!!!!!!!!!!!!!!!!!!!!!!!!!!!!!!!!!!!!!!!!!!!!!!!!!!!!!!!!!!!!!!!!!!!!!!!!!!!!!!!
*IF,ccafp_diameter,EQ,3,THEN
    !----------------------------------3mm dimensions-------------------------
    !outside diameter of the outer tube
    !0.259 inches
    d_out = 3.001 ! mm
    !d_out = 50.0 ! mm
    !inside diameter of the outer tube
    !d_in = 25.0 ! mm
    !0.239 inches
    d_in = 2.533 ! mm

    !inner flexure outside dimension
    !0.238 inches
    d2_out = 2.374! mm
    !0.218 inches
    d2_in = 1.944 ! mm
    !d2_in = 10.0 ! mm

    t = 0.125 !mm  flexure thickness

    !ansys param filename
    ansys_param_filename = 'ansys_param_3mm'
    !filename for the output file
    output_filename = 'ansys_output_3mm'

    !this was originally found below but is now found here
    ESIZE,0.055
    !moment = 0.9
    !moment = 1.8
    moment = 2.2


!!!!!!!!!!!!!!!!!!!!!!!!!!!!!!!!!!!!!!!!!!!!!!!!!!!!!!!!!!!!!!!!!!!!!!!!!!!!!!!
!!!!!!!!!!!!!!!!!!!!!!!!!!!!!!!!!!!!!!!!!!!!!!!!!!!!!!!!!!!!!!!!!!!!!!!!!!!!!!!
!!!!!!!!!!!!!!!!!!!!!!!!!!!!!!!!!!!!!!!!!!!!!!!!!!!!!!!!!!!!!!!!!!!!!!!!!!!!!!!
*ELSEIF,ccafp_diameter,EQ,5,THEN
    !----------------------------------5mm dimensions-------------------------
    !outside diameter of the outer tube
    d_out = 5.4991 !mm

    !inside diameter of the outer tube
    d_in = 4.89966 !mm


    !inner flexure outside dimension
    d2_out = 4.79806 !mm
```

```
    !inner flexure inside dimension
    d2_in = 4.04114 !mm

    t = 0.58139534883721*(d2_out-d2_in)/2.0 !mm  flexure thickness

    !ansys param filename
    ansys_param_filename = 'ansys_param_5mm'
    !filename for the output file
    output_filename = 'ansys_output_5mm'

    ESIZE,0.08
    moment = 4.2

!!!!!!!!!!!!!!!!!!!!!!!!!!!!!!!!!!!!!!!!!!!!!!!!!!!!!!!!!!!!!!!!!!!!!!!!!!!!
!!!!!!!!!!!!!!!!!!!!!!!!!!!!!!!!!!!!!!!!!!!!!!!!!!!!!!!!!!!!!!!!!!!!!!!!!!!
!!!!!!!!!!!!!!!!!!!!!!!!!!!!!!!!!!!!!!!!!!!!!!!!!!!!!!!!!!!!!!!!!!!!!!!!!!!
*ELSEIF,ccafp_diameter,EQ,8,THEN
    !---------------------------------8mm dimensions-----------------------------

    !outside diameter of the outer tube
    d_out = 7.99846 !mm

    !inside diameter of the outer tube
    d_in = 7.32282 !mm


    !inner flexure outside dimension
    d2_out = 6.9977 !mm

    !inner flexure inside dimension
    d2_in = 6.09854 !mm

    t = 0.58139534883721*(d2_out-d2_in)/2.0 !mm  flexure thickness

    !ansys param filename
    ansys_param_filename = 'ansys_param_8mm'
    !filename for the output file
    output_filename = 'ansys_output_8mm'

    ESIZE,0.125
    moment = 6.75


!!!!!!!!!!!!!!!!!!!!!!!!!!!!!!!!!!!!!!!!!!!!!!!!!!!!!!!!!!!!!!!!!!!!!!!!!!!!
!!!!!!!!!!!!!!!!!!!!!!!!!!!!!!!!!!!!!!!!!!!!!!!!!!!!!!!!!!!!!!!!!!!!!!!!!!!
!!!!!!!!!!!!!!!!!!!!!!!!!!!!!!!!!!!!!!!!!!!!!!!!!!!!!!!!!!!!!!!!!!!!!!!!!!!
*ELSE

*ENDIF


!this is all for the outside flexure
!minor outside axis of the outer flexure
min_out = d_out/2.0
!major outside axis of the outer flexure
maj_out = (d_out/2.0)/cos(beta)
```

```
!minor inside axis of the outer flexure
min_in = d_in/2.0
flexure_width = min_out - min_in

!maj_in = maj_out - flexure_width
!trying to get the flexure cross-section (which varies in a real cut tube)
maj_in = (d_in/2.0)/cos(beta)

!for the second flexure
!minor outside axis of the inner flexure
min2_out = d2_out/2.0
!major outside axis of the inner flexure
maj2_out =  (d2_out/2.0)/cos(beta)
!minor inside axis of the inner flexure
min2_in = d2_in/2.0
flexure2_width = min2_out - min2_in

!maj2_in = maj2_out - flexure2_width
!trying to get the flexure cross-section (which varies in a real cut tube)
maj2_in = (d2_in/2.0)/cos(beta)

!thickness now defined above
!t = 0.125 !mm  flexure thickness

b = min_out/3 !this is the length of one side of the rigid link to which the couple is
applied.

!this is so that we can scale the inner and outer ellipses to have the same
!flexure width throughout
scale_out = maj_out/min_out

!scale_in = (scale_out*min_out - flexure_width)/min_in
scale_in = maj_in/min_in

cyl4,0.0,0.0,min_out
arscale,1,,,1.0,scale_out,,,,1

cyl4,0.0,0.0,min_in
arscale,2,,,1.0,scale_in,,,,1

ASBA,1,2

!VOFFST,3,t/2,
!VOFFST,3,-t/2,

!second flexure

!the scale factor for the inside flexure

scale2_out = maj2_out/min2_out
!scale2_in = (scale2_out*min2_out - flexure2_width)/min2_in
scale2_in = maj2_in/min2_in
WPLANE,1,0.0,0.0,0.0,1.0,0.0,0.0,0.0,0.0,1.0

cyl4,0.0,0.0,min2_out
arscale,1,,,1.0,1.0,scale2_out,,,1
```

```
cyl4,0.0,0.0,min2_in
arscale,2,,,1.0,1.0,scale2_in,,,1

ASBA,1,2

!WPLANE,1,0.0,0.0,0.0,1.0,0.0,0.0,0.0,0.0,1.0
!WPOFFS,0.0,0.0,min_in*scale_in

VOFFST,3,t/2,
VOFFST,3,-t/2,
VADD,all

!VGLUE,1,2,
VSEL,NONE
VOFFST,4,t/2,
VOFFST,4,-t/2,
VADD,all
ALLSEL,all

!VGLUE,3,4,




! cut that large flexure at the same level as the small flexure inside dimension.
WPLANE,1, 0,0,0, 1,0,0, 0,0,1
WPOFFS,0.0,0.0,-(min2_in*scale2_in+.01)
VSBW,all
ASEL,s,loc,z,-t/2
!ASEL,r,loc,
VSLA,s,0
VADD,all
*GET,outside_flexure_vol,VOLU,0,num,max
ALLSEL,all
!VGLUE,5,6,7,8


!cut the small flexure
WPLANE,1, 0,0,0, 1,0,0, 0,1,0
WPOFFS,0,0,(min2_in*scale2_in+.01)
VSBW,all
ASEL,s,loc,y,-t/2
!ASEL,r,loc,
VSLA,s,0
VADD,all
*GET,inside_flexure_vol,VOLU,0,num,max
ALLSEL,all
!WPCSYS,-1
!VGLUE,1,2,9,10

!select the two keypoints on the outside flexure
LSEL,s,loc,y,(min2_in*scale2_in+.01)
LSEL,r,loc,z,t/2
```

```
KSLL,s
*GET,kp_x_max,KP,0,MXLOC,X
*GET,kp_x_min,KP,0,MNLOC,X
KSEL,r,loc,x,kp_x_max
*GET,kp_1,KP,0,NUM,MAX
ALLSEL,all
LSEL,s,loc,y,(min2_in*scale2_in+.01)
LSEL,r,loc,z,t/2
KSLL,s
KSEL,r,loc,x,kp_x_min
*GET,kp_2,KP,0,NUM,MAX
ALLSEL,all

!select the two keypoints on the inside flexure
LSEL,s,loc,z,(min2_in*scale2_in+.01)
LSEL,r,loc,y,t/2
KSLL,s
*GET,kp_x_max,KP,0,MXLOC,X
*GET,kp_x_min,KP,0,MNLOC,X
KSEL,r,loc,x,kp_x_min
*GET,kp_3,KP,0,NUM,MAX
ALLSEL,all
LSEL,s,loc,z,(min2_in*scale2_in+.01)
LSEL,r,loc,y,t/2
KSLL,s
KSEL,r,loc,x,kp_x_max
*GET,kp_4,KP,0,NUM,MAX
ALLSEL,all

!creates the coupler bottom area
A,kp_1,kp_2,kp_3,kp_4

!create the hardpoint for the off axis loading condition
!note that this also does not work, I'm guessing the line is regenerated without
!LSEL,NONE
!KSEL,s,KP,,kp_2,
!KSEL,a,KP,,kp_3,
!LSLK,s,1
!*GET,side_line,LINE,0,NUM,MAX
!KSEL,NONE
!HPTCREATE,LINE,side_line,,RATIO,0.5
!*GET,off_axis_load_point,KP,0,NUM,MAX
!ALLSEL,all

KSEL,s,loc,y,maj_out
KSEL,r,loc,z,t/2
*GET,kp_outside_tip,KP,0,NUM,MAX
LSLK,s,0
LSEL,r,loc,z,t/2
KSLL,s
LSLK,s,1
AL,all
ALLSEL,all

KSEL,s,loc,z,maj2_out
KSEL,r,loc,y,t/2
```

```
*GET,kp_inside_tip,KP,0,NUM,MAX
LSLK,s,0
LSEL,r,loc,y,t/2
KSLL,s
LSLK,s,1
AL,all
ALLSEL,ALL

!create line across the top section of the model
!LSEL,NONE
L,kp_outside_tip,kp_inside_tip
!*GET,apex_line,LINE,0,NUM,MAX
!create the hardpoint for the off axis loading condition -- note that this is not quite
centered, but i think that will be ok
!note that this does not work because the line on which the hardpoint is created goes away
later on...
!KSEL,NONE
!HPTCREATE,LINE,apex_line,,RATIO,0.5
!*GET,off_axis_load_point,KP,0,NUM,MAX
!ALLSEL,ALL


!create the two curved areas
KSEL,s,KP,,kp_outside_tip,
KSEL,a,KP,,kp_2,
KSEL,a,KP,,kp_3,
KSEL,a,KP,,kp_inside_tip,
LSLK,s,1
AL,all
ALLSEL,all

KSEL,s,KP,,kp_outside_tip,
KSEL,a,KP,,kp_inside_tip,
KSEL,a,KP,,kp_4,
KSEL,a,KP,,kp_1,
LSLK,s,1
AL,all
ALLSEL

!create the top volume that rigidly connects the two flexures
ASLV,
ASEL,INVE
VA,all
VSLA,s,1
*GET,coupler_vol,VOLU,0,num,max
ALLSEL,all

VGLUE,outside_flexure_vol,coupler_vol

KSEL,s,KP,,kp_outside_tip,
KSEL,a,KP,,kp_inside_tip,
KSEL,a,KP,,kp_4,
KSEL,a,KP,,kp_1,
LSLK,s,1
ASLL,s,1
VSLA,s,0
```

```
*GET,coupler_vol,VOLU,0,num,max
ALLSEL,all

VGLUE,inside_flexure_vol,coupler_vol

KSEL,s,KP,,kp_outside_tip,
KSEL,a,KP,,kp_inside_tip,
KSEL,a,KP,,kp_4,
KSEL,a,KP,,kp_1,
LSLK,s,1
ASLL,s,1
VSLA,s,0
*GET,coupler_vol,VOLU,0,num,max
ALLSEL,all


!L,51,59
!L,52,60
!L,18,42
!AL,9,86,10,104
!AL,9,84,49,102
!AL,10,103,49,85
!VA,21,22,4,40,13
!VGLUE,2,5,3

!the post to which the couple is applied
!K,,0,0,0
!K,,0,(min_in*scale_in)/2+.01,(min_in*scale_in)/2+.01
!K,,0,(min_in*scale_in+t)/2,(min_in*scale_in+t)/2
!square post cross section
KSEL,NONE
ASEL,NONE
K,,b/2,(min2_in*scale2_in+t)/2+b/2*cos(pi/4),(min2_in*scale2_in+t)/2 -b/2*cos(pi/4)
*GET,kp_5,KP,0,NUM,MAX
K,,b/2,(min2_in*scale2_in+t)/2-b/2*cos(pi/4),(min2_in*scale2_in+t)/2+b/2*cos(pi/4)
*GET,kp_6,KP,0,NUM,MAX
K,,-b/2,(min2_in*scale2_in+t)/2+b/2*cos(pi/4),(min2_in*scale2_in+t)/2-b/2*cos(pi/4)
*GET,kp_7,KP,0,NUM,MAX
K,,-b/2,(min2_in*scale2_in+t)/2-b/2*cos(pi/4),(min2_in*scale2_in+t)/2+b/2*cos(pi/4)
*GET,kp_8,KP,0,NUM,MAX

A,kp_5,kp_6,kp_8,kp_7,
*GET,moment_area,AREA,0,NUM,MAX
ALLSEL,all

!K,,5,(min_in*scale_in+t)/2-5*cos(pi/4),(min_in*scale_in+t)/2+5*cos(pi/4)
!K,,-5,(min_in*scale_in+t)/2+5*cos(pi/4),(min_in*scale_in+t)/2-5*cos(pi/4)
!K,,-5,(min_in*scale_in+t)/2-5*cos(pi/4),(min_in*scale_in+t)/2+5*cos(pi/4)
!A,63,64,66,65

!the key points that make up the line along which the rigid body will be extruded. The
pressure couple will be applied on this rigid body
!K,,0,0,0
K,,0,(min2_in*scale2_in+t)/2,(min2_in*scale2_in+t)/2
!K,,0,maj_out,maj_out
K,,0,sqrt((5*b+sqrt(2*(maj_out)**2))**2/2),sqrt((5*b+sqrt(2*(maj_out)**2))**2/2)
```

```
*GET,beam_top,KP,0,NUM,MAX

!KSEL,s,loc,x,0
!KSEL,r,loc,y,0
!KSEL,r,loc,z,0
KSEL,s,loc,x,0
KSEL,r,loc,y,(min2_in*scale2_in+t)/2
KSEL,r,loc,z,(min2_in*scale2_in+t)/2
*GET,line_start,KP,0,NUM,MAX
ALLSEL,all
!create the off axis load node
!NKPT,,line_start
!KSEL,s,KP,,line_start
!NSLK,s,line_start
!*GET,off_axis_load_node,NODE,0,NUM,MAX
!ALLSEL,all

KSEL,s,loc,x,0
KSEL,r,loc,y,sqrt((5*b+sqrt(2*(maj_out)**2))**2/2)
KSEL,r,loc,z,sqrt((5*b+sqrt(2*(maj_out)**2))**2/2)
*GET,line_end,KP,0,NUM,MAX
ALLSEL,all
LSEL,NONE
L,line_start,line_end
*GET,extrude_path,LINE,0,NUM,MAX
!HPTCREATE,LINE,extrude_path,,COORD,0.0,(min2_in*scale2_in+t)/2,(min2_in*scale2_in+t)/2
KSEL,NONE
HPTCREATE,LINE,extrude_path,,RATIO,0.001
*GET,off_axis_load_point,KP,0,NUM,MAX
ALLSEL,all
!K,,0,25.0,25.0

!K,,0,95.7106781187,95.7106781187
!L,62,68



VSEL,NONE
VDRAG,moment_area,,,,,,extrude_path,
*GET,moment_vol,VOLU,0,num,max
ALLSEL,all

VADD,coupler_vol,moment_vol,

!the following two sets of commands are used to define the area (really a volume) on which
the lower pressure is applied
WPLANE,1, 0,0,0, 1,0,0, 0,1,-1
!WPOFFS,0,0,25.3553390593
WPOFFS,0,0,sqrt(2*(maj_out)**2)-b
VSBW,all

WPLANE,1, 0,0,0, 1,0,0, 0,1,-1
!WPOFFS,0,0,35.3553390593
WPOFFS,0,0,sqrt(2*(maj_out)**2)
VSBW,all
```

```
!the following command is used to define the area on which the upper pressure is applied
WPLANE,1, 0,0,0, 1,0,0, 0,1,-1
!WPOFFS,0,0,125.355339059
WPOFFS,0,0,sqrt(2*(maj_out)**2)+4*b
VSBW,all

VSEL,s,loc,x,-min_in/2,min_in/2
VSEL,r,loc,y,-min_in/2,min_in/2
VSEL,r,loc,z,-min_in/2,min_in/2
VSEL,INVE
VADD,ALL
ALLSEL,all
!VGLUE,
!VGLUE,4,11,13,3

!create the hardpoint for the off axis loading condition
!KSEL,s,KP,,kp_1,
!KSEL,a,KP,,kp_2,
!KSEL,a,KP,,kp_3,
!KSEL,a,KP,,kp_4,
!LSLK,s,1
!ASLL,s,1
!*GET,coupler_bottom_area,AREA,0,num,max
!ALLSEL,all


!!!-----------add the radii to reduce stress concentrations---------------!!!
!cylinder diameter
!fillet_rad = 0.025
!VSEL,all
!CM,keep_vol,volu
!WPLANE,,min_out,0,0,min_out,1,0,min_out,0,1
!!CYL4,t/2,(min2_in*scale2_in+.01),0.009,,,,-d_out
!!CYL4,(min2_in*scale2_in+.01),t/2,0.009,,,,-d_out
!CYL4,t/2+fillet_rad,(min2_in*scale2_in+.01),fillet_rad,,,,-d_out
!CYL4,(min2_in*scale2_in+.01),t/2+fillet_rad,fillet_rad,,,,-d_out
!CMSEL,s,keep_vol,volu
!VSEL,inve
!CM,sub_vol,volu
!ALLSEL,all
!VSBV,keep_vol,sub_vol

!!!------------------------------------------------------------------------!!!

!!!------------------split model in half and use symmetry-----------------!!!
WPLANE,1, 0.0, 0.0, 0.0, 0.0, 1.0, 0.0, 0.0, 0.0, 1.0
VSBW,all,SEPO,DELETE
VSEL,s,loc,x,0.0,-maj_out
VDELE,all,,,1
ALLSEL,all

!!!----------------------------------MESHING-----------------------------!!!
!the following is used to select when the stress concentrations are
!VSEL,s,loc,x,-min_in/2,min_in/2
!VSEL,r,loc,y,-min_in/2,min_in/2
!VSEL,r,loc,z,-min_in/2,min_in/2
```

```
VSEL,s,loc,x,-min_out/2,min_out/2
VSEL,r,loc,y,-min_out/2,min_out/2
VSEL,r,loc,z,-min_out/2,min_out/2

!meshing parameters for the flexures -- see the setup for each size for the ESIZE command
!ESIZE,0.125
!ESIZE,0.06
MSHKEY,0
MSHAPE,1,3d
VMESH,all
!VMESH,1,2,
!VMESH,5,10,1

!meshing the rest of the beam
VSEL,INVE
ESIZE,1.0
VMESH,all
!VMESH,3,4
!VMESH,11
!VMESH,13
ALLSEL,all
!!!-----------------------------------------------------------------------------!!!
!!!!!!!!!!!!!!!!!!!!!!!!!!!!!!!!!!!!!!!!!!!!!!!!!!!!!!!!!!!!!!!!!!!!!!!!!!!!!!!
!!!!!!!!!!!!!!!!!!!!!!!!!!!!!!!!!!!!!!!!!!!!!!!!!!!!!!!!!!!!!!!!!!!!!!!!!!!!!!!

!apply symmetry constraint
ASEL,s,loc,x,0.0
DA,all,SYMM
ALLSEL,all

!select the nodes that will be fixed
!NSEL,s,LOC,Y,-scale_in*min_in,-scale_out*min_out
NSEL,s,LOC,Y,-scale2_in*min2_in,-maj_out
NSEL,a,LOC,Z,-scale2_in*min2_in,-maj2_out
!NPLOT
D,ALL,ALL,0
ALLSEL,ALL



!select the nodes that will be displaced
!NSEL,s,LOC,Y,scale_out*min_out,
!NPLOT
!D,ALL,UZ,d_out/1.5
!ALLSEL,ALL
!SFA,21,,PRES,-2.0
!LSWRITE,1

!number of load steps to run
steps = 20
!desired moment in N*mm divided by 2 because of symmetry
!3mm
!moment = 1.8/2.0
!5mm
!moment = 13.0/2.0
```

```
!8mm
!moment = 10.0/2.0
!moment arm in mm
L = 5*b
!area over which the pressure acts in mm^2 divided by 2
!A = b**2/2
!note that in the half model we will still use the full area to determine the correct
!pressure to apply because the model will apply the same pressure to half the area and the
!ccafp will have half the stiffness.
A = b**2

!force equivalent of the applied moment
F = 3*moment/L

!ASEL,s,loc,x,0
ASEL,s,loc,x,0,b/2.0
ASEL,r,loc,z,sqrt((sqrt(2*(maj_out)**2))**2/2),sqrt(b+(sqrt(2*(maj_out)**2))**2/2)
*GET,lower_face,AREA,0,NUM,MAX
ALLSEL,all

!ASEL,s,loc,x,0
ASEL,s,loc,x,0,b/2.0
ASEL,r,loc,y,sqrt((4.5*b+sqrt(2*(maj_out)**2))**2/2),sqrt((5*b+sqrt(2*(maj_out)**2))**2/2)
ASEL,r,loc,z,sqrt((4*b+sqrt(2*(maj_out)**2))**2/2),sqrt((4.5*b+sqrt(2*(maj_out)**2))**2/2)
*GET,upper_face,AREA,0,NUM,MAX
ALLSEL,all

!name the area that will be used for the buckling load.
ASEL,s,loc,x,0,b/2.0
ASEL,r,loc,y,sqrt((5*b+sqrt(2*(maj_out)**2))**2/2)
ASEL,r,loc,z,sqrt((5*b+sqrt(2*(maj_out)**2))**2/2)
*GET,top_face,AREA,0,NUM,MAX
ALLSEL,all

*GET,kp_outside_y,KP,kp_outside_tip,loc,Y
*GET,kp_outside_z,KP,kp_outside_tip,loc,Z
*GET,kp_inside_y,KP,kp_inside_tip,loc,Y
*GET,kp_inside_z,KP,kp_inside_tip,loc,Z
R_out = sqrt(kp_outside_y**2 + kp_outside_z**2)
R_in = sqrt(kp_inside_y**2 + kp_inside_z**2)


d_theta = (pi/4)/steps

*DO,i,1,steps,1
    !SFA,2,,PRES,4.0/4.0*i
    !SFA,40,,PRES,4.0/4.0*i

    !below is what we normally use (a pressure applied on the moment arm)
    SFA,lower_face,,PRES,((moment/(A*L))/steps)*i
    SFA,upper_face,,PRES,((moment/(A*L))/steps)*i

    !just a single follower force
    !SFA,upper_face,,PRES,((0.18/A)/steps)*i
```

```
    !simulating a cable pulling on the mechanism
    !FK,kp_inside_tip,FY,-F/(steps*sqrt(2))*i
    !FK,kp_inside_tip,FZ,-F/(steps*sqrt(2))*i


    !dout_y = R_out*cos(d_theta*i) - kp_outside_y
    !dout_z = R_out*sin(d_theta*i) - kp_outside_z
    !din_y = -(R_in*sin(d_theta*i) - kp_inside_y)
    !din_z = R_in*cos(d_theta*i) - kp_inside_z


    !DK,kp_outside_tip,UY,dout_y
    !DK,kp_outside_tip,UZ,dout_z
    !DK,kp_inside_tip,UY,din_y
    !DK,kp_inside_tip,UZ,din_z


    LSWRITE,i
*ENDDO

!!!----------------------------unload the CCAFP----------------------!!!
!!!!!!!!!!!!!!!!!!!!!!!!!!!!!!!!!!!!!!!!!!!!!!!!!!!!!!!!!!!!!!!!!!!!!!!
!!!!!!!!!!!!!!!!!!!!!!!!!!!!!!!!!!!!!!!!!!!!!!!!!!!!!!!!!!!!!!!!!!!!!!!
!this is to try to see the superelastic hysteresis
*DO,i,steps+1,2*steps+1,1
    !SFA,2,,PRES,4.0/4.0*i
    !SFA,40,,PRES,4.0/4.0*i

    !below is what we normally use (a pressure applied on the moment arm)
    SFA,lower_face,,PRES,moment/(A*L) - ((moment/(A*L))/steps)*(i-steps)
    SFA,upper_face,,PRES,moment/(A*L) - ((moment/(A*L))/steps)*(i-steps)

    !simulating a cable pulling on the mechanism
    !FK,kp_inside_tip,FY,-F/(steps*sqrt(2))*i
    !FK,kp_inside_tip,FZ,-F/(steps*sqrt(2))*i


    !dout_y = R_out*cos(d_theta*i) - kp_outside_y
    !dout_z = R_out*sin(d_theta*i) - kp_outside_z
    !din_y = -(R_in*sin(d_theta*i) - kp_inside_y)
    !din_z = R_in*cos(d_theta*i) - kp_inside_z


    !DK,kp_outside_tip,UY,dout_y
    !DK,kp_outside_tip,UZ,dout_z
    !DK,kp_inside_tip,UY,din_y
    !DK,kp_inside_tip,UZ,din_z


    LSWRITE,i
*ENDDO



!off axis stiffness loading condition-----------------------------------------------
!!off_axis = 0.9
```

```
    !ASEL,s,loc,x,0
    !ASEL,r,loc,y,(min2_in*scale2_in+t)/2-t,(min2_in*scale2_in+t)/2+t
    !ASEL,r,loc,z,(min2_in*scale2_in+t)/2-t,(min2_in*scale2_in+t)/2+t

    !KSEL,NONE
    !KSEL,s,KP,kp_1,
    !KSEL,a,KP,kp_2,
    !KSEL,a,KP,kp_3,
    !KSEL,a,KP,kp_4
    !LSLK,s,1
    !ASLL,s,1
    !*GET,coupler_bottom_area,AREA,0,num,max
    !ALLSEL,all

    !hpt_create,AREA,  ,,COORD,0,(min2_in*scale2_in+t)/2,(min2_in*scale2_in+t)/2
    !!*DO,i,1,steps,1

    !!  D,off_axis_load_point,UX,off_axis/steps*i

    !!  LSWRITE,i
    !!*ENDDO


    !-------------------------------------------------------------------------------

    !buckling loading condition-----------------------------------------------------
    buckling_load = 10
    *DO,i,1,steps,1
        SFA,top_face,,PRES,((buckling_load/A)/steps)*i
        LSWRITE,i
    *ENDDO

    !!!!!!!!!!!!!!!!!!!!!!!!!!!!!!!!!!!!!!!!!!!!!!!!!!!!!!!!!!!!!!!!!!!!!!!!!!!!
    !!!!!!!!!!!!!!!!!!!!!!!!!!!!!!!!!!!!!!!!!!!!!!!!!!!!!!!!!!!!!!!!!!!!!!!!!!!!
    !!!!!!!!!!!!!!!!!!!!!!!!!!!!!!!!!!!!!!!!!!!!!!!!!!!!!!!!!!!!!!!!!!!!!!!!!!!!
FINISH

!!!---------------------------------SOLUTION--------------------------------------!!!
/SOLVE

ANTYPE,0
NLGEOM,1
NSUBST,2,1000,1
!OUTRES,ERASE
!OUTRES,ALL,ALL

!loading the flexure only
LSSOLVE,1,steps,1

!loading and unloading the flexure
!LSSOLVE,1,2*steps+1,1

FINISH

!!!-----------------------------POSTPROCESSING-----------------------------------!!!
/POST1
```

```
!find the rotation angle
NSEL,s,loc,y,maj_out
NSEL,r,loc,z,0.0
NSEL,r,loc,x,0.0
!NSLL,s,1
!NSEL,r,loc,x,-L2
*GET,node1,NODE,0,num,max
*GET,node1y0,NODE,node1,loc,y
*GET,node1z0,NODE,node1,loc,z
ALLSEL,ALL

NSEL,s,loc,z,maj2_out
NSEL,r,loc,y,0.0
NSEL,r,loc,x,0.0
*GET,node2,NODE,0,num,max
*GET,node2y0,NODE,node2,loc,y
*GET,node2z0,NODE,node2,loc,z
ALLSEL,all

!Calculate Rotation of Jaw Tip
*GET,nod1y,NODE,node1,U,y
*GET,nod1z,NODE,node1,U,z
nd1y = node1y0+nod1y
nd1z = node1z0+nod1z

*GET,nod2y,NODE,node2,U,y
*GET,nod2z,NODE,node2,U,z
nd2y = node2y0+nod2y
nd2z = node2z0+nod2z
ALLSEL,ALL


len1 = sqrt((nd2y - nd1y)**2 + (nd2z - nd1z)**2)
len2 = sqrt((node2y0 - node1y0)**2 + (node2z0 - node1z0)**2)
!len2 = sqrt((node2y0 - node1y0)**2 + (node2z0 - node2y0)**2)

!output the needed parameters used to calculate the rotation in python
*CREATE,scratch,gui
/OUTPUT,ansys_param_filename,'csv','K:/Current Students/Jason Dearden/cylaxis_ANSYS'
*VWRITE,'node1y0','node1z0','node2y0','node2z0','len1','len2','steps','moment','modulus'
%C, %C, %C, %C, %C, %C, %C, %C, %C
*VWRITE,node1y0,node1z0,node2y0,node2z0,len1,len2,steps,moment,modulus
%G, %G, %G, %G, %G, %G, %G, %G, %G
/OUTPUT,TERM
*END
/INPUT,scratch,gui



rotation = acos(((nd2y - nd1y)*(node2y0 - node1y0) + (nd2z - nd1z)*(node2z0 - node1z0))/((len1)*
(len2)))*180/pi
!rotation = atan((nd2z-nd1z)/(nd2y-nd1y))*180./pi
!rotation2 = atan2((nd2z-nd1z),(nd2y-nd1y))*180./pi

!node with the maximum final stress
```

```
NSORT,S,EQV,0,0,1,SELECT
*GET,max_stress_node,NODE,0,NUM,MAX
*GET,max_von_mises,NODE,max_stress_node,S,EQV
ALLSEL,ALL

!----------------center of rotation calculations--------------------------------

NSEL,s,loc,y,maj_in
NSEL,r,loc,z,0.0
NSEL,r,loc,x,0.0
*GET,node3,NODE,0,num,max
*GET,node3y0,NODE,node3,loc,y
*GET,node3z0,NODE,node3,loc,z
ALLSEL,ALL

NSEL,s,loc,z,maj2_in
NSEL,r,loc,y,0.0
NSEL,r,loc,x,0.0
*GET,node4,NODE,0,num,max
*GET,node4y0,NODE,node4,loc,y
*GET,node4z0,NODE,node4,loc,z
ALLSEL,all


!-------------------------------------strain-----------------------------------------
NSORT,EPTO,EQV,0,0,1,SELECT
*GET,max_strain_node,NODE,0,num,max
!total equivalent (von mises) strain
*GET,max_strain,NODE,max_strain_node,EPTO,EQV
ALLSEL,all


!------------------------i don't think this is necessary; just use FSUM-------------------
!calculate the total reaction force in the
!make alist of all the selected nodes
NSEL,s,LOC,Y,-scale2_in*min2_in,-maj_out
NSEL,a,LOC,Z,-scale2_in*min2_in,-maj2_out

*DIM,rx_sum,array,steps,

*DO,i,1,steps,1
SET,i
!sample
!RFORCE,2,657,F,X, FX_2
!STORE,MERGE
FSUM
*GET,rx_sum(i),FSUM,0,ITEM,FX
!RFORCE,2,r_nodes[i],F,X, FX_2
!STORE,MERGE

!rx =
!rx_sum = rx_sum + rx
*ENDDO
ALLSEL,all
!
!*CFOPEN,'ansys_off_axis','csv','C:\Users\dartsum\Desktop'
```

```
!*CFOPEN,'C:\Users\dartsum\Desktop\ansys_off_axis','csv',,
!*VWRITE,rx_sum,
!(F18.10)
!*CFCLOSE

!the following code opens the ansys_off_axis.csv (and creates it if it does not exist)
!and writes the rx_sum array
!*
*CREATE,ansuitmp
*CFOPEN,'ansys_off_axis','csv',' '
*VWRITE,rx_sum(1,1,1), , , , , , , , ,
(F18.10',')
*CFCLOS
*END
/INPUT,ansuitmp
!*



FINISH

!!!-----------------time history postprocessing--------------------------!!!
/POST26

!FILE,'ccafp_ansys','rst','.'
!jobname is defined at the beginning of the file. notice that there are no quotes because it is
a variable, not a string
FILE,jobname,'rst','.'
/UI,COLL,1
NUMVAR,200
SOLU,91,NCMIT
STORE,MERGE
FILLDATA,91,,,,1,1
REALVAR,91,91
FORCE,TOTAL
!*
ANSOL,2,max_stress_node,S,EQV,SEQV_2
STORE,MERGE
!*
NSOL,3,node1,U,Y,UY_3,
STORE,MERGE
!*
NSOL,4,node1,U,Z,UZ_4,
STORE,MERGE
!*
NSOL,5,node2,U,Y,UY_5,
STORE,MERGE
!*
NSOL,6,node2,U,Z,UZ_6,
STORE,MERGE
!the two other points
!*
NSOL,7,node3,U,Y,UY_7,
STORE,MERGE
!*
NSOL,8,node3,U,Z,UZ_8,
```

```
STORE,MERGE
!*
NSOL,9,node4,U,Y,UY_9,
STORE,MERGE
!*
NSOL,10,node4,U,Z,UZ_10,
STORE,MERGE
!strain -- for some reason EPTO does not exist in POST26
!NSOL,11,max_strain_node,EPTO,EQV,EPTOEQV_11
!STORE,MERGE
!*
!von mises elastic strain
ANSOL,11,max_strain_node,EPEL,EQV,EPELEQV_11
STORE,MERGE

!*
!von mises plastic strain
ANSOL,12,max_strain_node,EPPL,EQV,EPPLEQV_12
STORE,MERGE


!filename for the output file
!output_filename = 'ansys_output_3mm'

! Save time history variables to file K:/Current Students/Jason Dearden/cylaxis_ANSYS/*.csv
*CREATE,scratch,gui
*DEL,_P26_EXPORT
*DIM,_P26_EXPORT,TABLE,steps,11
VGET,_P26_EXPORT(1,0),1
VGET,_P26_EXPORT(1,1),2
VGET,_P26_EXPORT(1,2),3
VGET,_P26_EXPORT(1,3),4
VGET,_P26_EXPORT(1,4),5
VGET,_P26_EXPORT(1,5),6
VGET,_P26_EXPORT(1,6),7
VGET,_P26_EXPORT(1,7),8
VGET,_P26_EXPORT(1,8),9
VGET,_P26_EXPORT(1,9),10
VGET,_P26_EXPORT(1,10),11
VGET,_P26_EXPORT(1,11),12
/OUTPUT,output_filename,'csv','K:/Current Students/Jason Dearden/cylaxis_ANSYS'
*VWRITE,'TIME','SEQV_2','UY_3','UZ_4','UY_5','UZ_6','UY_7','UZ_8','UY_9','UZ_10','EPELEQV_11','
EPPLEQV_12'
%C, %C, %C, %C, %C, %C, %C, %C, %C, %C, %C, %C
*VWRITE,_P26_EXPORT(1,0),_P26_EXPORT(1,1),_P26_EXPORT(1,2),_P26_EXPORT(1,3),_P26_EXPORT(1,4),
_P26_EXPORT(1,5),_P26_EXPORT(1,6),_P26_EXPORT(1,7),_P26_EXPORT(1,8),_P26_EXPORT(1,9),_P26_EXPORT
(1,10),_P26_EXPORT(1,11)
%G, %G, %G, %G, %G, %G, %G, %G, %G, %G, %G, %G
/OUTPUT,TERM
*END
/INPUT,scratch,gui
! End of time history save

FINISH
```

APPENDIX B. L-ARM FLEXURE FINITE ELEMENT CODE

The following code was used in the finite element analysis of a single flexure of the L-Arm mechanism. The code was written in the ANSYS Parametric Design Language (APDL) and run using a research licence of ANSYS 15.0. A pseudo moment was applied as a pressure on an area at the end of a rigid moment arm. The parametric model enables analysis at various scales. Stress, strain, and rotation values are output in post-processing.

```
FINISH
/CLEAR

/CWD,'C:\Users\dartsum\Desktop'

pi = acos(-1)

FINISH
/PREP7

    !beam_length = 1.0

    !6mm dimensions
    beam_length = 1.25
    !beam_width = 2.032

    !beam_height = 0.125
    !this is the smallest sheet thickness that we have found so far from nitinol.com
    !beam_height = 0.127
    beam_height = 0.1016
    beam_width = 0.25
    !length of the moment length
    scale = 10
    moment_length = scale*beam_length

    max_strain = 0.04
    ET,1,SOLID186
    !ET,1,BEAM188

    !material 1 properties
    MPTEMP,1,0
    !steel
    !MPDATA,EX,1,,200e9
    !polypropylene -- note that it is 10^3 -- this is because we are using mm (this value is in
    MPa and the stress out will be in MPa)
    !MPDATA,EX,1,,2e3
    !MPDATA,PRXY,1,,0.45
    !steel 304 is 193e3 MPa
    !nitinol modulus of elasticity
    MPDATA,EX,1,,44e3
    !MPDATA,EX,1,,200E3
    MPDATA,PRXY,1,,0.3

    !material 2 properties
    MPDATA,EX,2,,200E3
    MPDATA,PRXY,2,,0.3

    !shape memory material properties of NiTiNOL taken from the NDC values tabulated in
    "Compliant articulation
    !structure using superelastic NiTiNOL"
    TB,SMA,1,1,6,
    TBTEMP,0
    TBDATA,,440,472,218,206,0.045,0

    !SECTYPE,1,BEAM,RECT,,0
    !SECOFFSET,CENT
```

```
!SECDATA,beam_width,beam_height,0,0,0,0,0,0,0,0,0,0


K,1,0,0,0
K,2,0,beam_width,0
K,3,0,beam_width,beam_height
K,4,0,0,beam_height

A,1,2,3,4

k,5,beam_length,0,-beam_height
k,6,beam_length,beam_width,-beam_height
k,7,beam_length,beam_width,2*beam_height
k,8,beam_length,0,2*beam_height



A,5,6,7,8
!flexible portion
VOFFST,1,beam_length,
VSEL,all
VATT,1,,,
CM,sflp,VOLU
!create moment arm volume
VOFFST,2,moment_length
!create area for moment pressure
WPLANE,1, 0,0,0, 0,1,0, 0,0,1
WPOFFS,0.0,0.0,moment_length + beam_length/2.0
VSBW,all

!VGLUE,all
VSEL,all
!CMSEL,s,sflp
!CMSEL,a,marm
VGLUE,all
CMSEL,s,sflp
VSEL,invert
VATT,2,,,
CM,marm,VOLU
VSEL,all



!mesh the nitinol flexure
CMSEL,s,sflp
ESIZE,0.035
MSHKEY,0
MSHAPE,1,3d
!*
VMESH,all
!*

!mesh the rigid moment arm
CMSEL,s,marm
ESIZE,2.0
MSHKEY,0
```

```
    MSHAPE,1,3d
    !*
    VMESH,all
    !*

    !apply the fixed boundary condition.
    ASEL,s,loc,x,0.0
    DA,all,all,0.0
    ALLSEL,all

    steps = 20

    !preload condition
    f_preload = 0.0
    A_axial = 3.0*beam_height*beam_width
    ASEL,s,loc,x,(scale+1)*beam_length
    NSLA,s,1
    *GET,numnodes,NODE,0,COUNT
    F,all,FX,f_preload/numnodes*(i/steps)
    ALLSEL,all

    !bending loading condition
    !f_moment = 0.475
    f_moment = 0.5
    !f_moment = 5.0
    A_moment = (moment_length - beam_length/2.0)*beam_width
    *DO,i,1,steps,1
        !need to change this
        !DA,all,UZ,F/steps*i
        ASEL,s,loc,x,(scale+.75)*beam_length
        ASEL,r,loc,z,-beam_height
        SFA,all,1,PRES,f_moment/A_moment*(i/steps)
        ALLSEL,all

        LSWRITE,i
    *ENDDO

/REPLOT
FINISH

/SOLVE

    ANTYPE,0
    NLGEOM,1
    NSUBST,10,1000,1
    !OUTRES,ERASE
    !OUTRES,ALL,ALL
    LSSOLVE,1,steps,1

FINISH

/POST1

!------------------------------stress-------------------------------------
!NSORT,S,EQV,0,0,1,SELECT
NSEL,s,loc,x,beam_length/2.0
```

```
NSEL,r,loc,y,beam_width/2.0
NSEL,r,loc,z,beam_height/2.0
*GET,max_stress_node,NODE,0,NUM,MAX
*GET,max_von_mises,NODE,max_stress_node,S,EQV
ALLSEL,ALL

!-----------------------------------strain--------------------------------
!NSORT,EPTO,EQV,0,0,1,SELECT
!NSEL,s,loc,x,beam_length/2.0
!NSEL,r,loc,y,beam_width/2.0
!NSEL,r,loc,z,beam_height/2.0
!*GET,max_strain_node,NODE,0,num,max
!!total equivalent (von mises) strain
!*GET,max_strain_epto,NODE,max_strain_node,EPTO,EQV
!!equivalent elastic strain
!*GET,max_strain_epel,NODE,max_strain_node,EPEL,EQV
!ALLSEL,all

NSORT,EPTO,EQV,0,0,1,SELECT
*GET,max_strain_node,NODE,0,num,max
!total equivalent (von mises) strain
*GET,max_strain,NODE,max_strain_node,EPTO,EQV
ALLSEL,all

!-----------------------------reaction force-----------------------------
NSEL,s,loc,x,0.0
FSUM
ALLSEL,all

!-------------------------------rotation-----------------------------------

!find the rotation angle
NSEL,s,loc,x,moment_length + beam_length
NSEL,r,loc,y,0.0
NSEL,r,loc,z,2*beam_height
*GET,node1,NODE,0,num,max
*GET,node1x0,NODE,node1,loc,x
*GET,node1z0,NODE,node1,loc,z
ALLSEL,ALL

NSEL,s,loc,x,beam_length
NSEL,r,loc,y,
NSEL,r,loc,z,2*beam_height
*GET,node2,NODE,0,num,max
*GET,node2x0,NODE,node2,loc,x
*GET,node2z0,NODE,node2,loc,z
ALLSEL,all

!Calculate Rotation of Jaw Tip
*GET,nod1x,NODE,node1,U,x
*GET,nod1z,NODE,node1,U,z
nd1x = node1x0+nod1x
nd1z = node1z0+nod1z

*GET,nod2x,NODE,node2,U,x
*GET,nod2z,NODE,node2,U,z
```

```
nd2x = node2x0+nod2x
nd2z = node2z0+nod2z
ALLSEL,ALL


len1 = sqrt((nd2x - nd1x)**2 + (nd2z - nd1z)**2)
len2 = sqrt((node2x0 - node1x0)**2 + (node2z0 - node1z0)**2)

rotation = acos(((nd2x - nd1x)*(node2x0 - node1x0) + (nd2z - nd1z)*(node2z0 - node1z0))/((len1)*
(len2)))*180/pi
```